applied sciences

MDPI

Article

Mechanical Properties and Failure Mechanisms of Sandstone Influenced by Fracture Dip Angle and Fracture Number

Junhong Lian [1], Baolin Li [1,*], Zhonghui Li [2], Xiong Cao [1], Xiayan Zhang [2], Yiping Liu [1], Nan Liang [1], Meng Zhang [1,3] and Xuelong Li [4,*]

[1] School of Environment and Safety Engineering, North University of China, Taiyuan 030051, China; 13753179116@163.com (J.L.); cx92rl@163.com (X.C.); liu11121129@163.com (Y.L.); ln15034521948@163.com (N.L.); mzhang_cumt@163.com (M.Z.)
[2] School of Safety Engineering, China University of Mining and Technology, Xuzhou 221116, China; lizhonghui@cumt.edu.cn (Z.L.); xyzzhang@cumt.edu.cn (X.Z.)
[3] State Key Laboratory Cultivation Base for Gas Geology and Gas Control, Henan Polytechnic University, Jiaozuo 454003, China
[4] School of Energy and Mining Engineering, Shandong University of Science and Technology, Qingdao 266590, China
* Correspondence: baolinli234@126.com (B.L.); lixlcumt@126.com (X.L.)

Abstract

Fractures are widely developed in deep coal-mine surrounding rocks. They weaken the load-bearing capacity and energy-storage capacity of rock specimens, which may induce surrounding-rock deformation, roof collapse, and other hazards. Current studies on fractured rock masses mainly focus on a single parameter, such as fracture number or fracture dip angle. However, their coupled effects remain unclear. Integrated analyses of mechanical behavior, crack propagation, and energy evolution are also limited. In this study, uniaxial compression simulations of intact sandstone, single-fracture sandstone, and double-fracture sandstone were conducted using PFC^{2D}. The effects of fracture number and fracture dip angle on mechanical properties and failure characteristics were investigated. The results show that fractures reduced the peak stress and modulus of elasticity. A stronger weakening effect was observed with increasing fracture number. With increasing fracture dip angle, both peak stress and modulus of elasticity showed a V-shaped trend. The minimum peak stress occurred at 15°, while the minimum modulus of elasticity occurred at 45°. Sandstone failure was mainly dominated by tensile cracks. At 15°, the total crack number was the lowest, with 932 and 818 cracks for single-fracture and double-fracture specimens, respectively. Energy analysis showed that increasing fracture number reduced elastic strain energy and promoted dissipated energy. The weakest energy-storage capacity was observed at 30°. Overall, fracture number and fracture dip angle jointly controlled strength degradation, crack propagation, and energy evolution. This study provides a reference for fracture–damage assessment and disaster prevention in deep coal-bearing sandstone.

Keywords: uniaxial compression; sandstone; fracture dip angle; fracture number; force chain; PFC^{2D}

Check for updates

Received: 25 May 2026
Revised: 15 June 2026
Accepted: 21 June 2026
Published: 24 June 2026

Copyright: © 2026 by the authors. Licensee MDPI, Basel, Switzerland. This article is an open access article distributed under the terms and conditions of the Creative Commons Attribution (CC BY) license.

1. Introduction

As coal mining extends to greater depths, roadways surrounding rocks are subjected to high in situ stress, human-induced disturbance, and complex structural planes. Under these coupled conditions, the risks of surrounding-rock instability and disasters induced

by rapid energy release increase significantly [1–4]. Sandstone is a common lithology of roofs, floors, and roadways surrounding rocks in deep coal-bearing strata. Its load-bearing behavior and damage evolution directly affect roadway stability. Due to sedimentary diagenesis and tectonic modification, fractures with different numbers and orientations are commonly developed in sandstone [5]. These fractures affect the mechanical behavior, crack propagation paths, and energy evolution process. Therefore, a systematic investigation of the mechanical characteristics and failure mechanisms of fractured sandstone is of great theoretical significance and engineering value [6,7].

Current studies on the effects of fracture number and fracture dip angle on the mechanical properties of rock masses have mainly focused on the independent effect of a single factor. In terms of fracture number, an increase in fractures can weaken the structural integrity of rock masses. Stress concentration in the rock bridge region can also be enhanced. As a result, crack initiation, propagation, and coalescence show stronger spatial heterogeneity. The peak strength, elastic modulus, and overall load-bearing capacity are further reduced. Under multi-fracture conditions, the interaction between fractures is strengthened, and crack propagation paths become more complex. In terms of fracture dip angle, the relative relationship between the fracture plane and the principal stress direction is changed. Therefore, the crack initiation position, propagation direction, and tensile or shear failure mode are affected [8–11]. Wong et al. [12] conducted uniaxial compression tests on rock-like specimens containing three fractures. The effects of fracture arrangement, bridge angle, and frictional properties of fracture surfaces on crack coalescence mode and peak strength were revealed. Based on particle flow numerical simulations, Dai et al. [13] indicated that fracture dip angle and geometric configuration jointly affected crack coalescence mode and strength characteristics. It was also found that increasing fracture number further increased the complexity of rock failure. Lian et al. [14] performed biaxial compression tests on rock-like specimens containing double fractures. The effects of fracture dip angle, rock bridge angle, and lateral stress on crack propagation mode and strength characteristics were analyzed. These studies indicate that both fracture number and fracture dip angle affect the mechanical properties of rocks. However, the variation in rock mechanical properties under their combined effects remains unclear. Compared with a single-factor effect, the variations in mechanical parameters, such as peak strength and elastic modulus, are more complex under the combined effects of fracture dip angle and fracture number. The spatial evolution of crack initiation, propagation, and coalescence is also more difficult to characterize accurately. Therefore, a clear research gap remains in the evolution mechanism and influence laws of rock mechanical parameters under the coupled effects of these two factors. Systematic studies are still urgently needed.

The essential causes of macroscopic mechanical properties of rock masses, such as strength degradation, differences in crack propagation, and energy evolution, should often be explained from a mesoscopic perspective. Force chains are a key link between the mesoscopic load-bearing structure and the macroscopic mechanical response of rock masses. Therefore, they provide an effective approach for addressing this issue. Zhang et al. [15] showed that the formation of force chains directly affects the strength evolution of granular materials. It is also closely related to shear band formation and energy dissipation. Zhang et al. [16] analyzed the evolution of contact force networks and tensile force chains in rock-like cemented granular materials under different confining pressures based on DEM. The regulating effects of confining pressure on contact force distribution, crack formation, and the number and length of tensile force chains were revealed. Wang et al. [17] found through experiments that excavation disturbance can cause the reorganization of strong force chains and the formation of a bearing arch structure. This changes the stress transmission path in the granular system. McBeck et al. [18] indicated, based on DEM

simulations, that the spatial distribution of spanning force chains in porous granular rocks is closely related to crack propagation and macroscopic failure. The above studies mainly focused on intact rock specimens or granular systems without pre-existing fractures. The relationship between force chain evolution and macroscopic mechanical response was emphasized. However, the effects of pre-existing fractures on force chains and failure behavior have not been systematically considered. In contrast, force chain characteristics at peak stress are analyzed in this study. From the perspective of the mesoscopic load-bearing structure, the differences in sandstone failure behavior caused by the combined effects of fracture number and fracture dip angle are systematically investigated. The underlying causes of these differences are also clarified. This further reveals the mesoscopic origin of the sandstone failure mechanism under the coupled effects of fracture number and fracture dip angle.

In summary, previous studies have mainly revealed the mechanical characteristics and failure behavior of fractured rock masses with respect to individual factors, such as fracture number or fracture dip angle. However, the differences in the fracture–number effect under different fracture dip angles still need to be further clarified. In addition, the relationships among macroscopic mechanical properties, microcrack evolution, energy evolution, and the mesoscopic load-bearing skeleton in sandstone remain unclear. Therefore, intact, single-fracture, and double-fracture sandstone models were established using the particle flow method (PFC^{2D}). The peak strength, elastic modulus, microcrack evolution, and energy evolution characteristics of sandstone under different combinations of fracture number and fracture dip angle were analyzed. Compared with previous studies that mainly focused on a single fracture parameter or a single response index, the supplementary contribution of this study lies in two aspects. First, the variation in the fracture–number effect with fracture dip angle was quantitatively characterized using relative change rate and fitting analysis. Second, based on the force-chain distribution at the peak stress state, the fracture resistance index R and the local strong force-chain density ρ_s were used to further interpret the differences in strength degradation, microcrack evolution, and energy dissipation from the perspective of the mesoscopic load-bearing skeleton. The results can provide a reference for damage assessment, adverse fracture identification, and key support-zone determination in deep coal mine surrounding rocks.

2. Establishment of Numerical Models

2.1. PFC Simulation Methods and Constitutive Models

To investigate the mechanical properties and failure mechanisms of fractured sandstone under uniaxial compression at the mesoscale, numerical simulations were conducted using the Particle Flow Code (PFC), a discrete element method-based program. In PFC, rock materials are discretized into an assembly of rigid circular particles. Forces and moments are transmitted between particles through contact constitutive laws. The force, displacement, and failure evolution of the particle system are iteratively solved using an explicit dynamic relaxation algorithm. At each time step, contact forces are first updated based on relative particle displacements. Subsequently, the acceleration, velocity, and displacement of each particle are calculated according to the resultant forces and moments. Particle positions and contact states are then updated. The process proceeds to the next iteration until equilibrium is reached or failure occurs. This process is illustrated in Figure 1. Compared with laboratory experiments, PFC simulations can effectively reproduce crack initiation, propagation, and coalescence in rock under loading. They can also track mesoscopic cracks, contact forces, and post-peak failure behavior, which are difficult to observe directly in experiments. Therefore, PFC has been widely applied to the study of mesoscopic rock fracture mechanisms [19–22]. In addition, by adjusting particle geometry, contact properties,

and mesoscopic parameters, the macroscopic mechanical behavior of the numerical model can be matched with that of the target rock specimen [23,24].

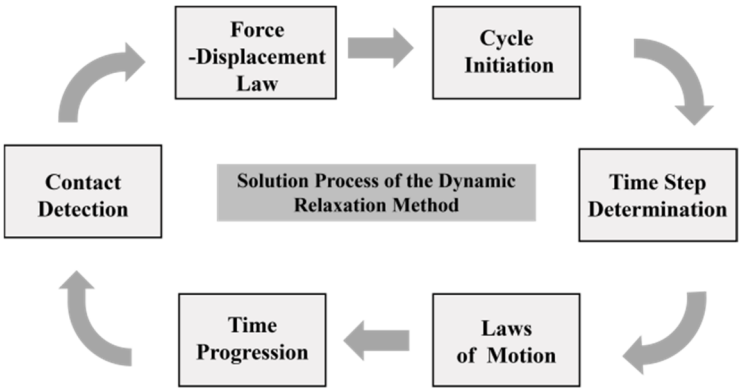

Figure 1. Schematic diagram of the dynamic relaxation method solution process.

The contact constitutive model determines the mesoscopic mechanical behavior of the particle system and is critical for discrete element simulations. Considering that the loading walls mainly provide boundary constraints and axial loading during uniaxial compression, a linear contact model was used between the loading walls and particles to simulate rigid boundary contact. A parallel bond model (PBM) was adopted between particles to represent the cementation between sandstone grains and its damage evolution. In the PBM, a finite-sized bonded cross-section is introduced at each particle contact. Thus, normal and shear forces, as well as corresponding moments, can be transmitted between particles. These interactions jointly resist particle opening, sliding, and rotation. Therefore, the PBM can effectively describe the interparticle bonding characteristics and bond breakage behavior of cemented brittle rocks. It should be noted that the standard built-in parallel-bond model in PFC^{2D} was directly used for the numerical calculations in this study. The software version used in this study was PFC^{2D} 5.00.25. No self-developed FISH or Python 3.14.6 scripts were used to implement the normal-stress, shear-stress, or failure-criterion calculations of the parallel-bond model. The following equations are only used to describe the basic mechanical relationships and failure criteria of this model.

In the parallel bond model, relative translation and rotation between particles generate normal force, shear force, and corresponding moments at the bonded cross-section. The parallel bond force $\overline{F}$ can be decomposed into normal and shear components. The parallel bond moment $\overline{M}$ is resolved into a twisting moment acting about the contact normal direction and a bending moment acting in the contact plane. The mathematical expressions of the parallel bond force and moment are given in Equations (1)–(3), respectively, as follows:

$$\overline{F} = -\overline{F}_n \hat{n} + \overline{F}_s \hat{t}_s \quad (1)$$

$$\overline{M} = \overline{M}_a \quad (2)$$

$$\overline{M}_a = \overline{M}_t \hat{n} + \overline{M}_b \hat{t}_s \quad (3)$$

In the formula: $\overline{F}_n$ $\overline{F}_s$ $\overline{M}_t$ $\overline{M}_b$ are the normal component of the parallel bond force, the shear component of the parallel bond force, the twisting moment, and the bending moment, respectively; $\overline{M}_a$ is the assigned value of the resultant moment of the parallel bond; $\hat{n}$ denotes the direction of the normal force; $\hat{t}_c$ and $\hat{t}_s$ indicate the principal tangential direction and the secondary tangential direction, respectively.

According to the failure criteria of the parallel joint model, the maximum normal stress and maximum shear stress at the bonded cross-section are calculated using Equations (4) and (5), respectively, as follows:

$$\overline{\sigma}_{max} = \frac{-\overline{F}_n}{\overline{A}} + \frac{|\overline{M}_b|R}{I} \tag{4}$$

$$\overline{\tau}_{max} = \frac{-\overline{F}_s}{\overline{A}} + \frac{|\overline{M}_t|R}{J} \tag{5}$$

In the formula: $\overline{\sigma}_{max}$, $\overline{\tau}_{max}$ are the principal stress and shear stress, respectively; $\overline{A}$ denotes the particle contact area; R represents the particle radius; I is the cross-sectional moment of inertia; J is the polar moment of inertia. For the PFC^{2D} model, the torsional degree of freedom is absent, and the polar moment of inertia J is generally replaced by the cross-sectional moment of inertia I.

When $\overline{\sigma}_{max}$ exceeds the tensile bond strength or $\overline{\tau}_{max}$ exceeds the shear bond strength, the parallel bonding fails; after failure, the contact between particles degrades from bonded contact to unbonded linear friction contact, as shown in Figure 2a,b. It can thus be seen that the PBM effectively describes the entire process of intergranular bonding in rock materials, from intact to damaged to ultimate failure.

In numerical simulations, the failure of parallel bonds directly corresponds to the initiation of microcracks. Specifically, when a bond fails due to excessive normal tensile stress, it is recorded as a tensile crack in the model. When a bond fails due to excessive shear stress, it is recorded as a shear crack, as shown in Figure 2c. As loading progresses, microcracks continuously initiate, propagate, and coalesce. This process is finally manifested as the crack evolution and instability failure of the specimen at the macroscale. Therefore, by monitoring the number and spatial distribution of different types of microcracks in real time, the effects of fracture number and fracture dip angle on the strength and deformation characteristics of sandstone can be analyzed. Their effects on energy evolution, local damage concentration, and final failure modes can also be further revealed. This provides a basis for the subsequent systematic analysis of the failure mechanism of fractured sandstone from multiple perspectives, including macroscopic mechanical properties, microcrack evolution, energy distribution, and force chain characteristics.

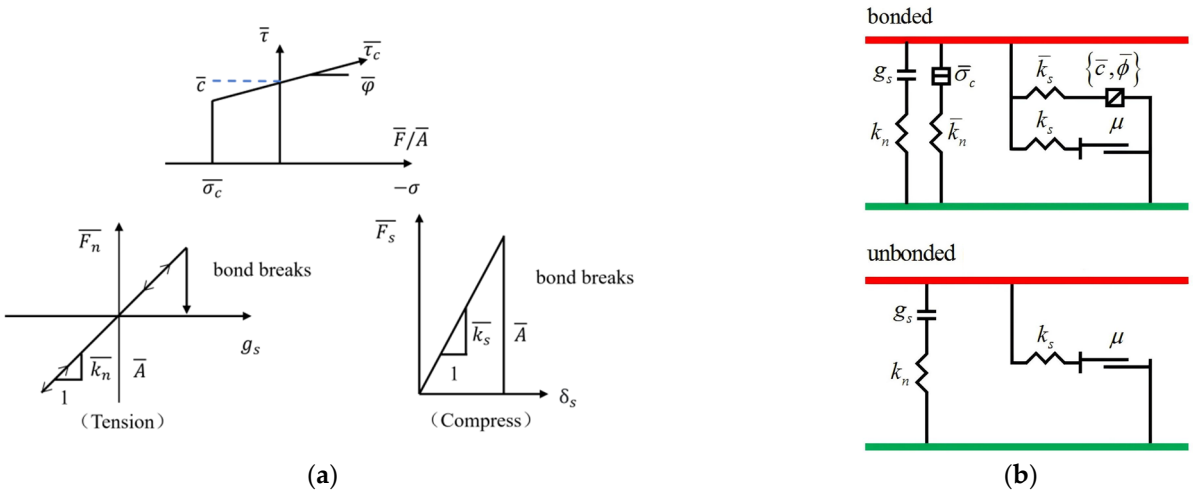

Figure 2. *Cont.*

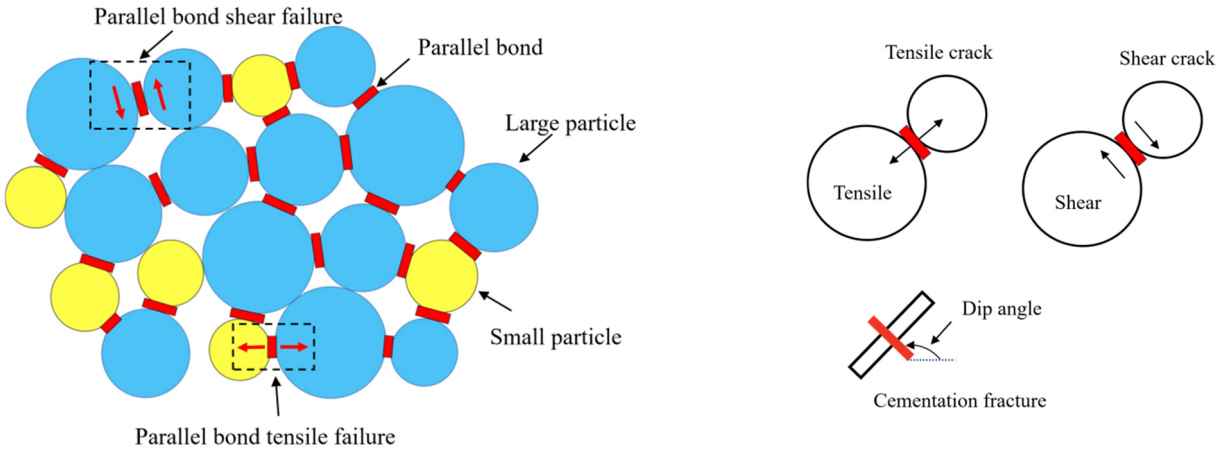

(**c**)

Figure 2. Schematic of particle failure modes, mechanical properties, and constitutive relationships in the parallel bonding model [25]. (**a**) Force–Displacement Relationship and Failure Envelope. (**b**) Constitutive Relations of Parallel Bonding Models. (**c**) PFC Particle Disruption Mode. g_s: contact area-related factor; $\overline{k}_n$: Normal stiffness; $\overline{k}_s$: stiffness; $\overline{\sigma}_c$: Bond strength; $\overline{c}$: cohesive force; $\overline{\varphi}$: Internal friction angle; μ: Coefficient of friction; $\overline{F}/\overline{A}$: Force per unit area; $\overline{\tau}$: Shear strength; $\overline{\tau}_c$: The magnitude of shear strength during the transition from brittle to ductile behavior in rock until failure; σ: Average Normal Stress; $\overline{F}$: The parallel bond force.

2.2. Parameter Calibration

In PFC^{2D}, a sandstone specimen with a height of 100 mm and a width of 50 mm was established. The minimum and maximum particle diameters were set as 0.30 mm and 0.48 mm, respectively, and a total of 8562 particles were generated. The sandstone was collected from Linyi City, Shandong Province, China. It is a fine-grained heterogeneous material with crystalline and massive structural characteristics, and its average bulk density is approximately 2650 kg/m^3 [26]. To ensure that the numerical model could reasonably reflect the macroscopic mechanical properties of sandstone, a trial-and-error method was used to calibrate the mesoscopic parameters of the model [27]. The calibrated mesoscopic parameter data are listed in Table 1. Specifically, the laboratory uniaxial compression test results were taken as the target, and mesoscopic parameters, including particle contact parameters, parallel bond parameters, and friction parameters, were repeatedly adjusted so that the stress–strain curve shape and peak stress obtained from the numerical simulation were in good agreement with the experimental results [28–31]. In this study, the peak stress of 190.8 MPa obtained from the laboratory uniaxial compression test was used as the main calibration basis, and the value ranges of mesoscopic parameters reported by Yang et al. [32] were also referenced. A uniaxial compression simulation was then conducted on the intact sandstone specimen. The simulated peak stress was 193.0 MPa, with a relative error of only 1.15% compared with the experimental value of 190.8 MPa, and the simulated stress–strain curve showed a similar overall trend to the experimental curve. This indicates that the selected mesoscopic parameters can reasonably reflect the macroscopic mechanical response of the sandstone. Based on the calibrated parameters, uniaxial compression models of intact, single-fracture, and double-fracture sandstone were further established to investigate the mechanical properties and failure characteristics under different fracture numbers and fracture dip angles. The prefabricated fracture dip angles were 0°, 15°, 30°, 45°, 60°, 75°, and 90°. To ensure the comparability among different fractured specimens, the single-fracture and double-fracture models used the calibrated mesoscopic material parameters of the intact sandstone model. Only the geometric structure of the specimens was changed by introducing pre-existing fractures. Since laboratory tests were not conducted for each

combination of fracture number and fracture dip angle in this study, the rationality of the fractured models is further discussed in Section 4.3 This discussion is based on comparisons with existing experimental results on fractured sandstone in terms of mechanical properties, crack propagation characteristics, and energy evolution behavior.

Table 1. The micro-parameters used in the PFC^{2D} model for brittle sandstone specimens.

Micro-Parameters	Values
Young's modulus of the particle, E_c (GPa)	24.25
Young's modulus of the parallel bond, $\overline{E}_c$ (GPa)	24.25
Parallel bond radius multiplier	1.0
Ratio of normal to shear stiffness of the particle, k_n/k_s	1.3
Ratio of normal to shear stiffness of the parallel bond, $\overline{k}_n/\overline{k}_s$	1.3
Particle friction coefficient, μ	0.35
Parallel bond normal strength, mean (MPa)	113
Parallel bond normal strength, standard deviation (MPa)	18.08
Parallel bond shear strength, mean (MPa)	180.08
Parallel bond shear strength, standard deviation (MPa)	29.93

2.3. Construction Method of the Double-Fracture Geometric Model

To investigate the influence of fracture inclination on the mechanical behavior of sandstone, two pre-existing fractures with the same length and orientation were constructed in the numerical model. The two fractures were arranged in parallel. To ensure a consistent geometric relationship under different inclination angles, their positions were determined based on central symmetry.

As shown in Figure 3, a two-dimensional Cartesian coordinate system was established with the specimen center as the origin. The centers of the two fractures were denoted as A and B, which were centrosymmetric about the origin. Half of the distance between the two fracture centers was defined as r. Thus, points A and B were located on a circle with radius r. Let the fracture inclination angle be θ. The coordinates of the two fracture centers can be expressed as A (r·sin θ, r·cos θ) and B (−r·sin θ, −r·cos θ). Therefore, the distance between the fracture centers remains constant at 2r during angular variation. Since both fractures are defined using the same inclination angle θ, their orientations remain identical, ensuring that the two fractures remain parallel. In the PFC model, points A and B were first calculated according to θ and 2r. Then, two fractures with the same length and orientation were generated using A and B as their centers. By changing θ, double-fracture specimens with different inclination angles were obtained.

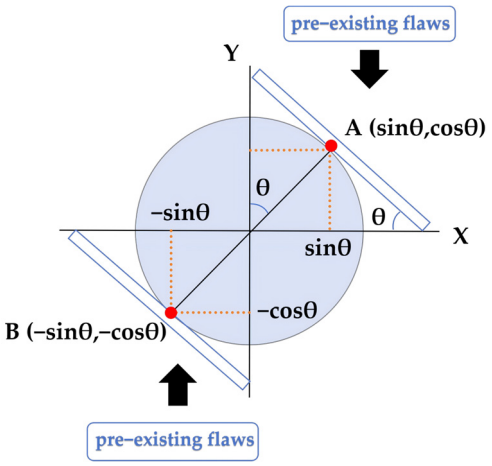

Figure 3. Schematic diagram of the double-slit method.

For illustrative purposes, r was set to 1 in Figure 3. In this case, the coordinates of A and B are simplified as A (sin θ, cos θ) and B (−sin θ, −cos θ). This method provides a consistent geometric basis for analyzing the influence of fracture inclination.

3. Results and Analysis

3.1. Macroscopic Mechanical Analysis

Uniaxial compression numerical simulations were conducted on intact sandstone, single-fracture sandstone, and double-fracture sandstone. The macroscopic mechanical responses of sandstone under different combinations of fracture number and fracture dip angle were investigated. Figure 4 shows the typical staged evolution during the whole uniaxial compression process, using the stress–strain curve of intact sandstone as an example. Overall, the compression failure process of rock can be divided into four stages: the compaction stage (AB), elastic deformation stage (BC), unstable fracture propagation stage (CD), and post-peak stage (DE).

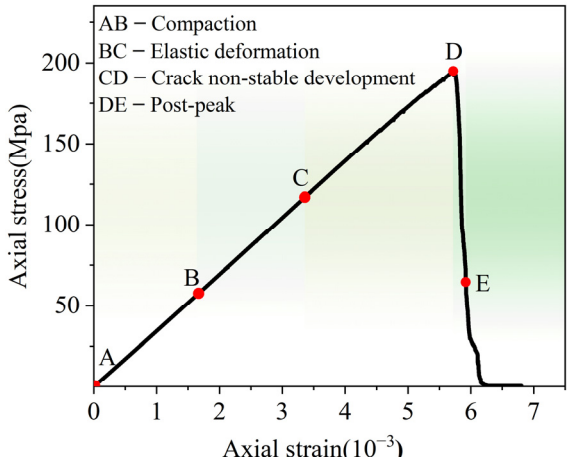

Figure 4. Stress–strain curve for unfractured sandstone.

During the compaction stage (AB), the initial pores and microfractures inside natural sandstone gradually close under low stress. Therefore, the macroscopic stress–strain curve usually shows a concave-up shape. However, the PFC numerical model used in this study is composed of rigid particles, and the compaction effect of natural pores is not considered. Thus, this stage is not significant in the curve. In the elastic deformation stage (BC), the curve increases approximately linearly with the continuous increase in axial stress. The specimen mainly undergoes recoverable elastic deformation, and the stress–strain relationship basically follows Hooke's law. When the stress exceeds the elastic limit, the specimen enters the unstable crack propagation stage (CD). At this stage, microcracks begin to initiate at particle contacts. These microcracks are mainly tensile cracks, accompanied by a small number of shear cracks. The number of microcracks increases rapidly with increasing stress, but a macroscopic coalesced failure plane has not yet formed through the specimen. After the stress reaches the peak strength, the specimen enters the post-peak stage (DE). Internal microcracks rapidly propagate and coalesce, forming a main fracture zone through the specimen. The stress drops sharply with increasing strain, showing typical brittle failure characteristics.

To reveal the evolution laws of the effects of fracture number and fracture dip angle on the macroscopic mechanical properties of sandstone, the peak strength and modulus of elasticity of single-fracture and double-fracture sandstone under different dip angles were statistically analyzed, as shown in Figure 5. Overall, both fracture number and fracture dip angle significantly affect the peak strength and deformation characteristics of sandstone,

and their effects on different mechanical parameters show clear differences. For single-fracture sandstone, the peak strength first decreases and then increases with increasing fracture dip angle, showing an overall V-shaped trend. When the fracture dip angles are 0° and 90°, the peak strength is 193 MPa, indicating a relatively high strength level. When the dip angle increases to 15°, the peak strength decreases to the minimum value of 125 MPa, which is only 64.8% of that of intact sandstone. With a further increase in fracture dip angle, the peak strength gradually recovers, indicating that the weakening effect of high-dip-angle fractures on the load-bearing capacity of sandstone is reduced. The modulus of elasticity of single-fracture sandstone ranges from 32.10 to 35.50 GPa. It also first decreases and then increases, reaching the minimum value of 32.10 GPa at a dip angle of 45°. Therefore, the degradation of peak strength in single-fracture sandstone is mainly concentrated at a dip angle of 15°, whereas a dip angle of 45° more easily causes initial stiffness degradation. This reflects the different effects of fracture dip angle on different macroscopic mechanical indices. For double-fracture sandstone, the peak strength also shows an approximately V-shaped trend with increasing dip angle. The peak strengths corresponding to dip angles of 0° and 90° are 177 MPa and 186 MPa, respectively, remaining at relatively high levels. At a dip angle of 15°, the peak strength decreases to the minimum value of 99 MPa. Under the same dip angle, the peak strength of double-fracture sandstone is significantly lower than that of single-fracture sandstone, indicating that an increase in fracture number further damages the internal structure of the specimen and weakens the integrity of the rock mass. Taking the 15°condition as an example, the peak strength of the double-fracture specimen decreased to 99 MPa, compared with 125 MPa for the single-fracture specimen. This value is only 51.3% of the strength of the intact sandstone. The results suggest that increasing fracture number enhances the interaction between fractures and further weakens the load-bearing structure. The corresponding mechanism is discussed in the following section based on the force-chain evolution characteristics. The modulus of elasticity of double-fracture sandstone is generally lower than that of single-fracture sandstone, ranging from 30.20 to 34.70 GPa. It also reaches the minimum value of 30.20 GPa at a dip angle of 45°. This indicates that an increase in fracture number not only reduces the peak load-bearing capacity of sandstone but also significantly weakens its overall stiffness, resulting in a further decrease in the deformation resistance of the specimen.

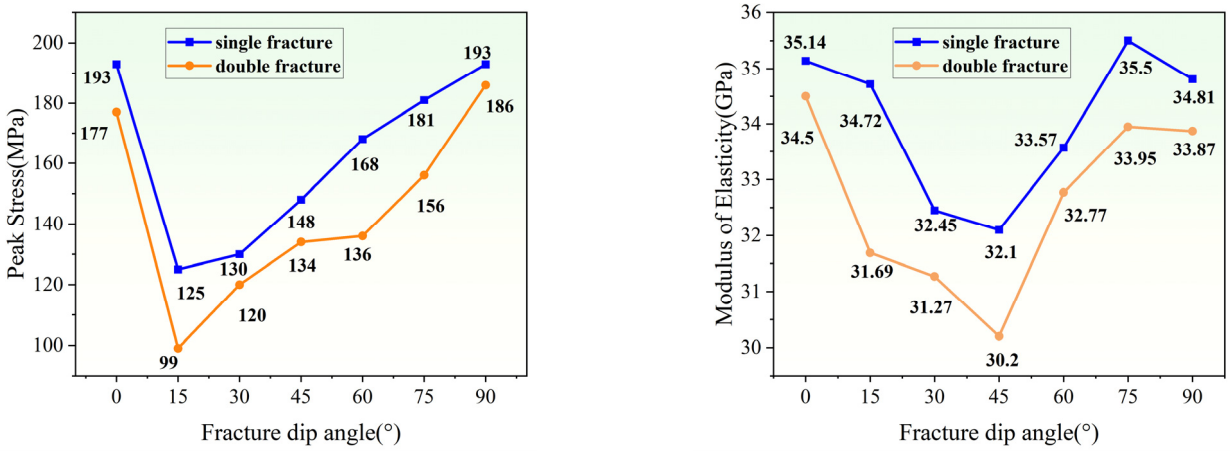

Figure 5. Variation in uniaxial compressive strength and elastic modulus with fracture dip angle.

Overall, the increase in fracture number mainly reduces the structural integrity of the specimen, resulting in an overall decrease in peak strength and modulus of elasticity. Fracture dip angle further controls the differences in the responses of different mechanical parameters. Under both single-fracture and double-fracture conditions, the peak strength

reaches its minimum value at 15°, whereas the modulus of elasticity reaches its minimum value at 45°. This indicates that the controlling effects of fracture dip angle on peak load-bearing capacity and initial stiffness are inconsistent.

3.2. Patterns of Microcrack Evolution

The macroscopic mechanical analysis above shows that both fracture number and fracture dip angle affect the peak strength and modulus of elasticity of sandstone. Moreover, the unfavorable dip angles corresponding to different mechanical parameters are not consistent. To further reveal the mesoscopic damage characteristics of sandstone after failure under different fracture numbers and dip angles, the microcrack number, crack types, and spatial distribution of single-fracture and double-fracture sandstone after failure were statistically analyzed. The results are shown in Figures 6 and 7. The post-failure microcrack number mainly reflects the final damage development of the specimen. The microcrack types can be used to characterize different damage modes, while the crack spatial distribution can be used to describe the degree of damage localization and the distribution characteristics of failure zones [33].

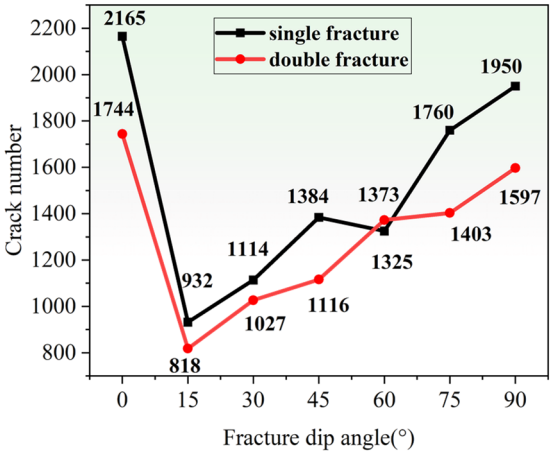

Figure 6. Changes in total microcracks in sandstone at different inclination angles.

In terms of microcrack types, all specimen groups are dominated by tensile cracks, whereas shear cracks account for a relatively low proportion. This indicates that tensile cracks dominate the failure process of fractured sandstone under uniaxial compression. In terms of fracture number, the total number of microcracks in double-fracture sandstone is generally lower than that in single-fracture sandstone under the same dip angle. Taking typical dip angles as examples, the total numbers of microcracks in single-fracture specimens are 2165, 932, 1384, and 1950 at 0°, 15°, 45°, and 90°, respectively, whereas those in double-fracture specimens are 1744, 818, 1116, and 1597, respectively. In both single-fracture and double-fracture specimens, the variation trend of tensile crack number with dip angle is basically consistent with that of the total crack number, while shear cracks always account for a small proportion in each group. This indicates that an increase in fracture number reduces the total number of post-failure microcracks, but does not fundamentally change the composition of microcrack types. Combined with the macroscopic mechanical results above, although the total number of post-failure microcracks in double-fracture specimens is smaller, their peak strength and modulus of elasticity are generally lower than those of single-fracture specimens. This suggests that an increase in fracture number does not necessarily lead to the generation of more new microcracks. Instead, it changes the failure characteristics of the specimen by reducing the initial structural integrity and enhancing local damage localization at the tips of pre-existing fractures.

In terms of fracture dip angle, the microcrack number of both single-fracture and double-fracture specimens generally first decreases and then increases. For single-fracture specimens, the total number of microcracks decreases significantly from 2165 at 0° to 932 at 15°, which is the lowest value among all dip angles. It then increases to 1114, 1384, and 1325 at 30°, 45°, and 60°, respectively, and further increases to 1760 and 1950 at 75° and 90°, respectively. A similar trend is observed in double-fracture specimens. The total number of microcracks reaches the minimum value of only 818 at 15°, whereas it reaches 1744 and 1597 at 0° and 90°, respectively. These results indicate that fracture dip angle significantly affects microcrack development. Both single-fracture and double-fracture specimens show a decreasing and then increasing trend in microcrack number with increasing dip angle. The lowest microcrack number at 15° indicates that crack development is more localized under this condition. In contrast, the higher microcrack numbers at 0° and 90° suggest that crack propagation is relatively more sufficient.

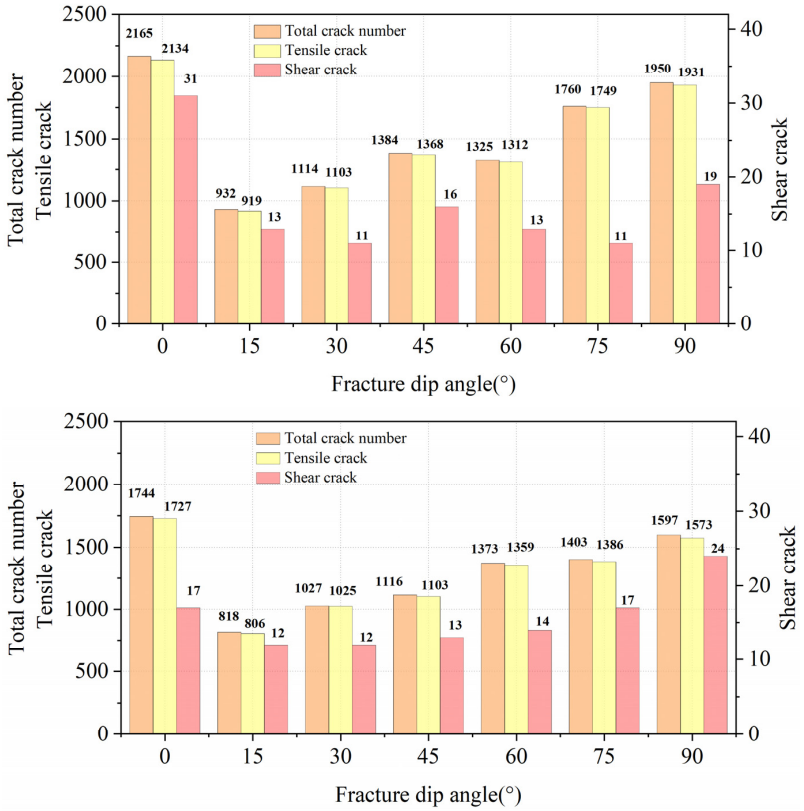

Figure 7. Number of cracks generated at different fracture dip angles.

The spatial distribution of microcracks further reflects the differences in damage localization under different fracture conditions. For single-fracture specimens, cracks are distributed over a relatively wide range at 0°, indicating that crack propagation is relatively sufficient after failure. At 15°, cracks are mainly concentrated around the pre-existing fracture, showing obvious localization characteristics. At 30–60°, the crack distribution range gradually expands, and the crack-affected zone is relatively wide at 45°. At 75° and 90°, the crack number further increases, and the distribution range also expands. For double-fracture specimens, cracks mainly develop around the tips of the two pre-existing fractures and their adjacent regions. The distribution range is more concentrated than that in single-fracture specimens, indicating that crack propagation under double-fracture conditions is more strongly controlled by the geometry of the pre-existing fractures.

Overall, fracture number and fracture dip angle have different effects on microcrack development, as shown in Figure 8. An increase in fracture number tends to promote

localized microcrack development around the tips of pre-existing fractures and their adjacent regions. It also imposes a stronger constraint on microcrack propagation. Therefore, double-fracture specimens exhibit more obvious mechanical degradation and damage localization despite a smaller number of post-failure microcracks. In contrast, fracture dip angle mainly affects the variation in microcrack number and the spatial distribution range of cracks, causing the specimens to show either localized or relatively dispersed damage characteristics under different dip angles. Therefore, the failure process of fractured sandstone is not controlled by a single fracture parameter, but results from the combined effects of fracture number and fracture dip angle.

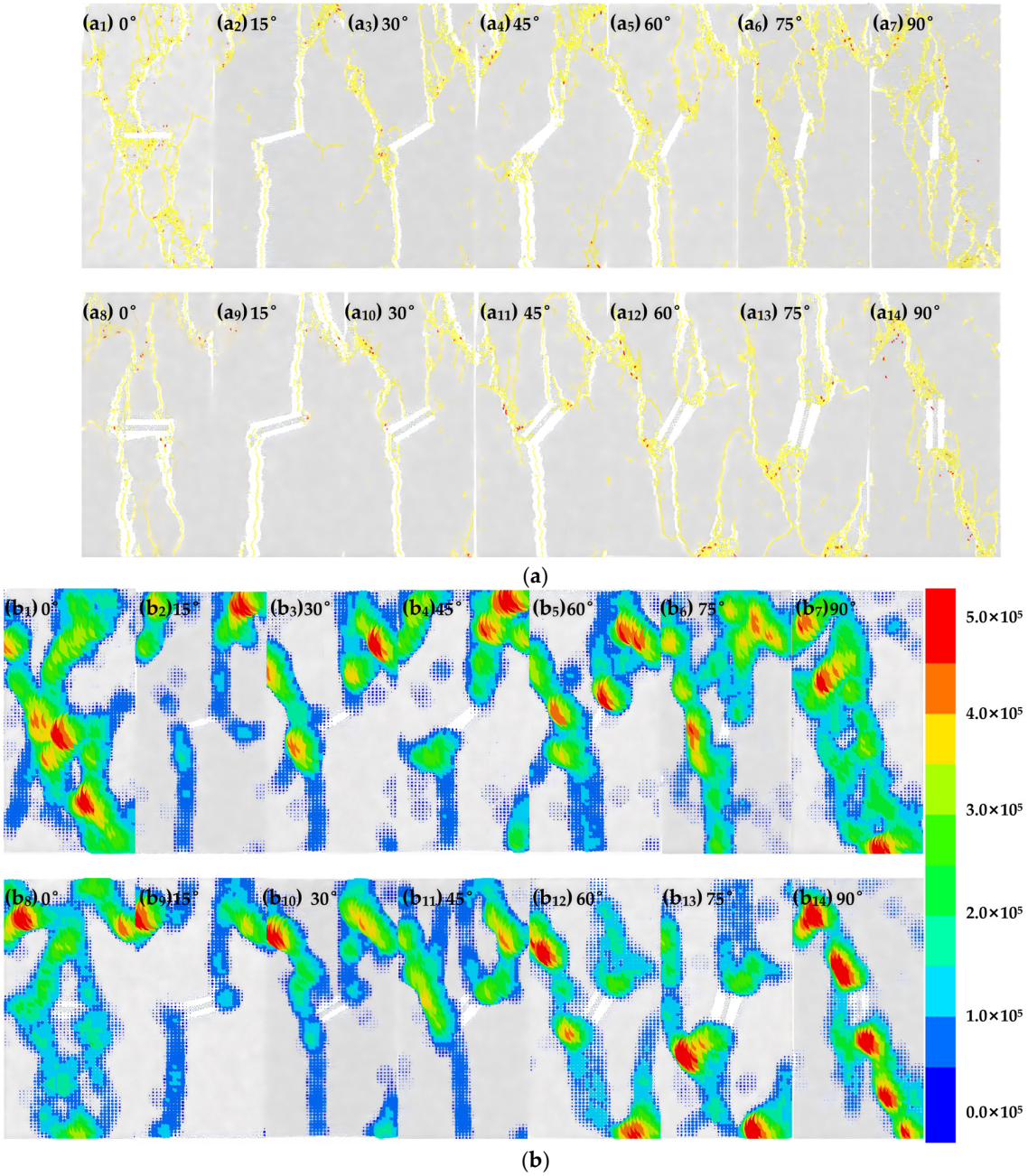

Figure 8. Microcrack distribution of fractured sandstones with different dip angles. (**a**) Microcrack distribution; ($\mathbf{a_1}$–$\mathbf{a_7}$) single-fracture specimens and ($\mathbf{a_8}$–$\mathbf{a_{14}}$) double-fracture specimens with dip angles of 0°, 15°, 30°, 45°, 60°, 75°, and 90°, respectively. (**b**) Microcrack hotspot distribution; ($\mathbf{b_1}$–$\mathbf{b_7}$) single-fracture specimens and ($\mathbf{b_8}$–$\mathbf{b_{14}}$) double-fracture specimens with dip angles of 0°, 15°, 30°, 45°, 60°, 75°, and 90°, respectively.

3.3. Patterns of Energy Evolution

The above analysis shows that fracture number and fracture dip angle not only significantly affect the peak strength and modulus of elasticity of sandstone, but also change the microcrack number and spatial distribution characteristics. However, macroscopic mechanical parameters and post-failure crack distributions mainly reflect the final failure state of the specimen. They are insufficient for further revealing the transformation mechanism between energy storage and damage dissipation during the pre-peak loading process. Therefore, it is necessary to analyze, from the perspective of energy evolution, the transition process of sandstone from stable energy storage to enhanced damage dissipation under different combinations of fracture number and fracture dip angle. In this study, the evolution laws of total energy, elastic strain energy, and dissipated energy of intact sandstone, single-fracture sandstone, and double-fracture sandstone under different dip angles were analyzed.

The uniaxial compression process of sandstone is essentially a process of continuous energy accumulation, distribution, and release. Under conditions where heat exchange between the specimen and the external environment is neglected, according to the first law of thermodynamics, all work performed by external forces during the deformation and failure of the rock is entirely converted into energy storage and dissipation. The total strain energy of the specimen can be expressed as in Equation (6) [34]:

$$U = U_e + U_d \tag{6}$$

In the equation: U represents the total absorbed energy; U_e represents the elastic strain energy; and U_d represents the dissipated energy that causes damage and fracture in the specimen. The formulas for the total energy, elastic strain energy, and dissipated strain energy are given in Equations (7)–(9) [35]:

$$U = \int \sigma_1 d\varepsilon_1 = \sum_{i=1}^{n} \frac{1}{2}(\sigma_1^i + \sigma_1^{i+1})(\varepsilon_1^{i+1} - \varepsilon_1^i) \tag{7}$$

$$U_e = \frac{1}{2}\sigma_1 \varepsilon_1^e = \frac{\sigma_1^2}{2E} \tag{8}$$

$$U_d = U - U_e \tag{9}$$

According to the first law of thermodynamics, the work performed by external forces is converted into energy storage and dissipation inside the specimen. Therefore, the total energy consists of elastic strain energy and dissipated energy, as expressed in Equation (6). The calculation methods for total energy, elastic strain energy, and dissipated energy are given in Equations (7)–(9), respectively, where σ_1 and ε_1 are the axial stress and axial strain, respectively, and E is the modulus of elasticity.

Figure 9 shows the evolution curves of total energy, elastic strain energy, and dissipated energy of single-fracture sandstone (a–g) and double-fracture sandstone (h–n) under different dip angles. Overall, the energy evolution of specimens under different fracture conditions shows similar staged characteristics. At the initial loading stage, total energy and elastic strain energy increase almost synchronously, whereas dissipated energy remains at a low level. This indicates that the external input energy is mainly stored inside the specimen in the form of elastic strain energy. As loading continues, dissipated energy gradually increases, indicating the initiation and development of local damage. Near the peak stress, the growth rate of dissipated energy increases significantly. This suggests that the stable load-bearing structure inside the specimen is gradually weakened, and damage propagation is enhanced. In the post-peak stage, elastic strain energy is rapidly released,

while dissipated energy increases sharply and eventually tends to stabilize. This indicates that the specimen changes from a pre-peak stage dominated by energy storage to a post-peak stage dominated by damage dissipation. However, under different combinations of fracture number and fracture dip angle, the timing and intensity of the transition between energy storage and dissipation are different. This suggests that fracture geometry further affects the internal energy storage and damage dissipation processes of the specimen.

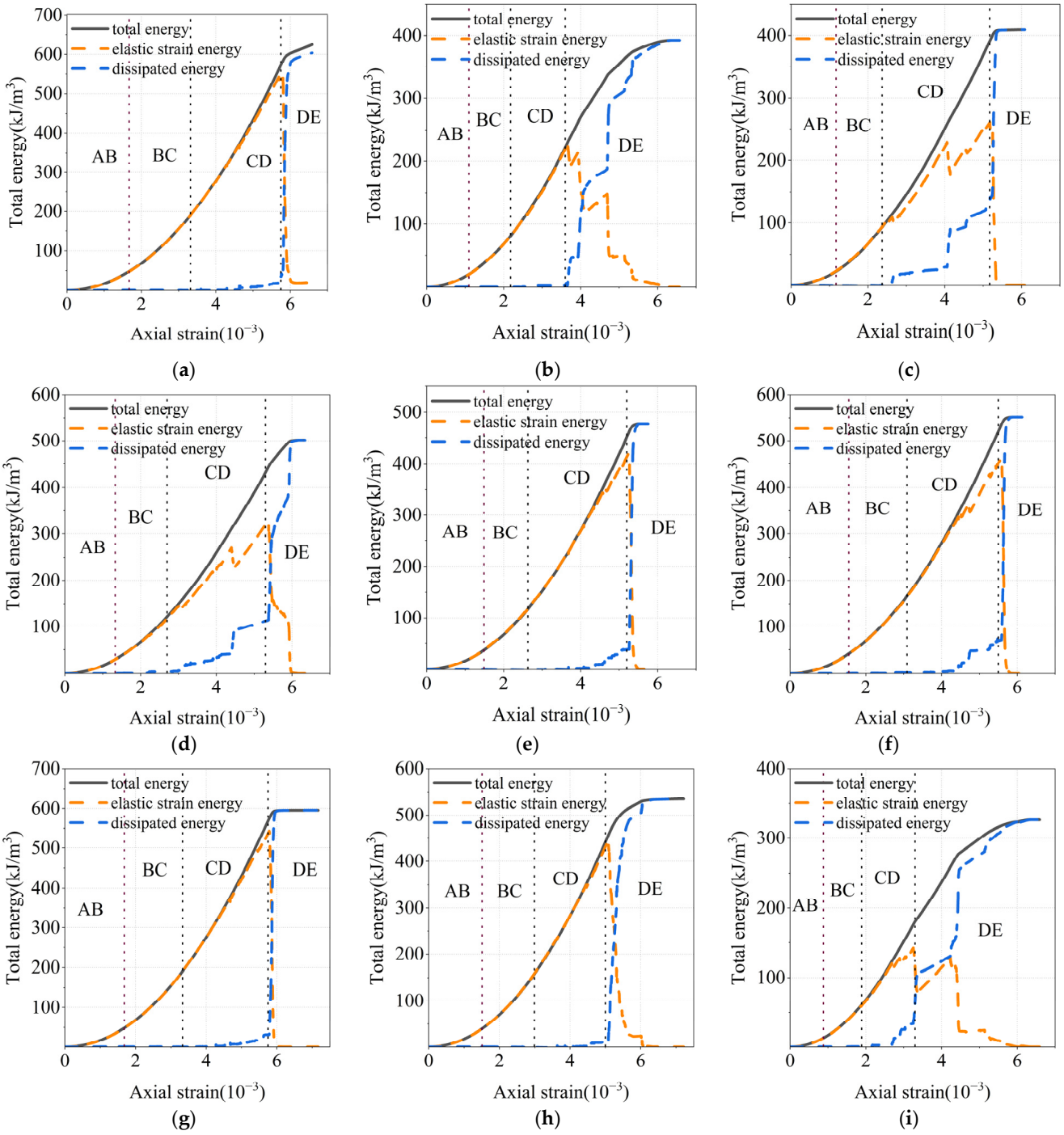

Figure 9. *Cont.*

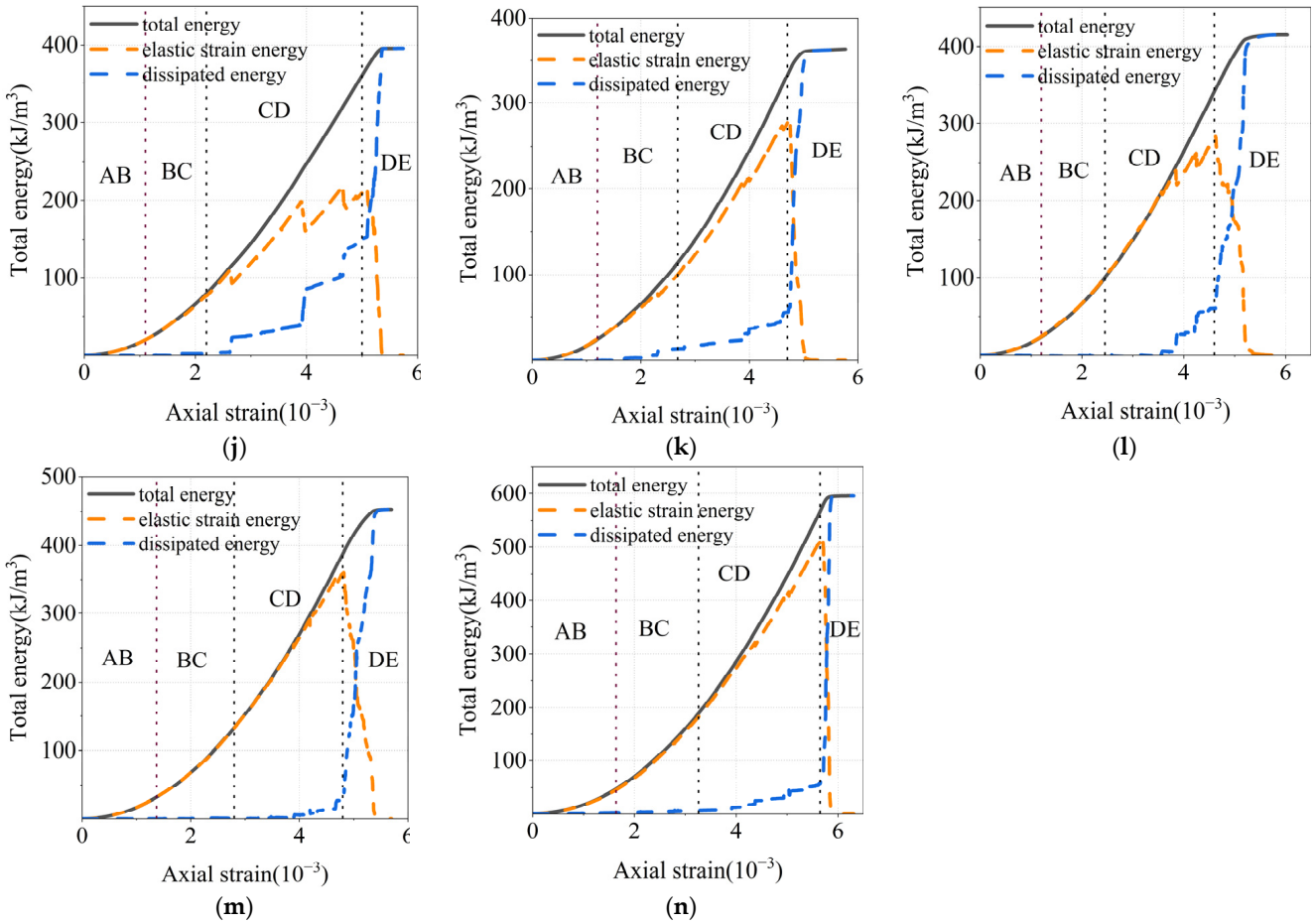

Figure 9. Energy evolution characteristics of sandstone specimens with different fracture dip angles. (**a**) θ_{single} = 0°, (**b**) θ_{single} = 15°, (**c**) θ_{single} = 30°, (**d**) θ_{single} = 45°, (**e**) θ_{single} = 60°, (**f**) θ_{single} = 75°, (**g**) θ_{single} = 90°, (**h**) θ_{double} = 0°, (**i**) θ_{double} = 15°, (**j**) θ_{double} = 30°, (**k**) θ_{double} = 45°, (**l**) θ_{double} = 60°, (**m**) θ_{double} = 75°, (**n**) θ_{double} = 90°.

To further quantitatively characterize the energy storage and dissipation characteristics of specimens at the peak state under different fracture combinations, the total energy at the peak point, elastic strain energy at the peak point, and the ratio indices U_e/U and U_d/U_e were selected as characterization parameters to reflect the pre-peak energy storage capacity and damage dissipation characteristics of the specimens. The elastic strain energy ratio at the peak point (U_e/U) reflects the proportion of input energy stored in the form of elastic strain energy before the peak stress. A higher value indicates stronger pre-peak energy storage capacity and lower damage dissipation. The ratio of dissipated energy to elastic strain energy at the peak point of the stress–strain curve (U_d/U_e) is defined as the brittleness index modification coefficient (BIM). This coefficient can be used to characterize the pre-peak dissipation degree and relative ductility characteristics of rocks. A larger value indicates stronger pre-peak damage dissipation and relatively more obvious ductility characteristics of sandstone [36]. The energy parameters at the peak point of the stress–strain curve are listed in Table 2.

From the perspective of fracture number, the stable pre-peak energy storage capacity of the specimens generally weakens with increasing fracture number. For intact sandstone, the total energy and elastic strain energy at the peak point are 572 kJ/m^3 and 546 kJ/m^3, respectively. The U_e/U value is 0.95, whereas the U_d/U_e value is only 0.05, indicating that the intact specimen can maintain strong energy storage capacity and a low damage dissipation level before the peak stress. Under most dip-angle conditions, the total energy

and elastic strain energy at the peak point of double-fracture specimens are lower than those of the corresponding single-fracture specimens. For example, at 0°, the total energy and elastic strain energy at the peak point of the single-fracture specimen are 572 kJ/m^3 and 537 kJ/m^3, respectively, whereas those of the double-fracture specimen decrease to 456 kJ/m^3 and 437 kJ/m^3, respectively. At 60°, the corresponding values of the single-fracture specimen are 461 kJ/m^3 and 419 kJ/m^3, respectively, whereas those of the double-fracture specimen further decrease to 345 kJ/m^3 and 281 kJ/m^3, respectively. These results indicate that increasing fracture number significantly reduces the elastic strain energy that can be maintained before the peak stress, thereby weakening the energy basis required for stable load-bearing. For engineering surrounding rock, this suggests that rock masses under multi-fracture conditions may be less capable of maintaining the energy accumulation required for stable load-bearing and may exhibit a reduction in bearing stability at an earlier stage. It should be noted that the energy parameters listed in Table 2 do not show a strict linear relationship with the final total number of microcracks presented in the previous section. This is because the total number of microcracks mainly reflects the damage extent after specimen failure, whereas the energy parameters describe the characteristics of energy accumulation, storage, and dissipation during the loading process. For fractured sandstone, the presence of pre-existing fractures changes the initiation, propagation, and coalescence paths of cracks. As a result, crack growth tends to occur along existing weak planes, leading to macroscopic failure. Therefore, energy evolution is affected not only by the number of microcracks but also by crack propagation patterns, fracture interactions, and local stress redistribution. Consequently, the variation in energy parameters is not necessarily consistent with that of the final total number of microcracks. From the perspective of fracture dip angle, fracture dip angle mainly regulates the distribution of input energy between elastic energy storage and damage dissipation. For single-fracture specimens, the U_e/U values at 0° and 90° are both 0.94, which are the highest among all dip angles, whereas the value decreases to the minimum value of 0.67 at 30°. Correspondingly, the U_d/U_e value at 30° increases to 0.50, which is significantly higher than the value of 0.07 at 0° and 90°. Double-fracture specimens exhibit a similar trend. The U_e/U value reaches the maximum value of 0.96 at 0°, whereas it decreases to 0.57 at 30°, which is the minimum value among all double-fracture conditions. Meanwhile, the U_d/U_e value at 30° reaches 0.75, which is the highest among all dip angles. These results indicate that, under the 30° condition, the input energy in both single-fracture and double-fracture specimens is more difficult to be continuously and stably stored in the form of elastic strain energy. Instead, the energy is more likely to be dissipated before the peak stress through crack initiation, propagation, and local damage evolution. Therefore, the specimens enter the enhanced damage dissipation stage earlier. For engineering surrounding rock, this indicates that fracture combinations at 30° are more unfavorable for stable pre-peak load-bearing and are more likely to form an energy evolution state unfavorable to surrounding-rock stability.

Overall, fracture number and fracture dip angle play significantly different roles in the energy evolution of sandstone. Increasing fracture number mainly weakens the pre-peak elastic energy storage capacity of the specimen, resulting in a reduction in the elastic strain energy that can be maintained at the peak stage. Fracture dip angle further regulates the distribution of input energy between elastic energy storage and damage dissipation. Under the 30°condition, both single-fracture and double-fracture specimens exhibit relatively low U_e/U values and high U_d/U_e values, indicating that the proportion of input energy converted into elastic strain energy is relatively low, whereas pre-peak damage dissipation is relatively strong. As a result, the specimens are more likely to enter the enhanced damage dissipation stage earlier. Combined with the previous results, 15° mainly corresponds to peak load-bearing capacity degradation, 45° mainly corresponds to initial stiffness

deterioration, whereas 30° corresponds to stronger pre-peak damage dissipation. This indicates that the influence of fracture dip angle on the failure process of sandstone is not concentrated in a single mechanical index, but exhibits differentiated responses in terms of strength, stiffness, crack development, and energy dissipation.

Table 2. Peak energy parameters of specimens with fractures at different dip angles.

Number of Fractures	Angle	Total Energy at Peak Point (kJ/m^3)	U_e (kJ/m^3)	U_e/U	U_d (kJ/m^3)	U_d/U_e	Total Energy (kJ/m^3)
0	/	572	546	0.95	26	0.05	601
1	0°	572	537	0.94	35	0.07	623
	15°	261	213	0.82	48	0.23	392
	30°	390	260	0.67	130	0.50	410
	45°	439	325	0.74	114	0.35	501
	60°	461	419	0.91	42	0.10	477
	75°	531	461	0.87	70	0.15	551
	90°	574	537	0.94	37	0.07	595
2	0°	456	437	0.96	19	0.04	534
	15°	263	212	0.81	51	0.24	392
	30°	371	212	0.57	159	0.75	395
	45°	335	279	0.83	56	0.20	362
	60°	345	281	0.81	64	0.23	415
	75°	389	358	0.92	31	0.09	453
	90°	578	514	0.89	64	0.12	594

4. Discussion

4.1. Coupling Effect of Fracture Number and Dip Angle

The preceding sections analyzed the influence of fracture number and fracture dip angle on the failure behavior of sandstone from the perspectives of macroscopic mechanical properties, microcrack evolution, and energy distribution. The results indicate that the strength characteristics, crack propagation behavior, and energy dissipation laws of sandstone exhibit significant differences under different combinations of fracture number and fracture dip angle. To further reveal the coupling effect between fracture number and fracture dip angle, it is necessary to quantitatively compare the differences between single-fracture and double-fracture specimens under the same fracture dip angle. If the differences between single-fracture and double-fracture specimens remain approximately constant under different dip-angle conditions, this indicates that the influence of fracture number is less dependent on fracture dip angle. In contrast, if the differences vary significantly with fracture dip angle, this suggests that fracture number and fracture dip angle exhibit significant coupling effects. Based on this, relative change rates (η) are employed to quantitatively characterize the differences between single-fracture and double-fracture specimens under different dip angles. In this study, uniaxial compressive strength (UCS), elastic modulus (E), microcrack number (N_c), elastic strain energy ratio (U_e/U), and dissipation-to-storage energy ratio (U_d/U_e) are selected as evaluation indices. The relative change rate (η) is defined according to Equation (10):

$$\eta(\theta) = \frac{M_{single}(\theta) - M_{double}(\theta)}{M_{single}(\theta)} \times 100\% \quad (10)$$

In the equation, $M_{single}(\theta)$ and $M_{double}(\theta)$ represent the corresponding values of the evaluation index for single-fracture and double-fracture specimens under a fracture dip angle θ, respectively. When $\eta > 0$, this indicates that the value of the parameter decreases for double-fracture specimens relative to single-fracture specimens. When $\eta < 0$, the value of the parameter increases for double-fracture specimens relative to single-fracture specimens.

If the relative change rates of each parameter vary only slightly with fracture dip angle, this suggests that the coupling effect between fracture number and fracture dip angle is relatively weak. In contrast, if the relative change rates vary significantly with fracture dip angle, this indicates that a significant coupling effect exists between fracture number and fracture dip angle.

According to the relative change rates of each index listed in Table 3, the effects of fracture number and fracture dip angle on the failure behavior of sandstone are not independent. The relative change rate of peak strength is the highest at 15° and 60°, reaching 20.80% and 19.05%, respectively, and is the lowest at 90°, with a value of only 3.63%. This indicates that the weakening effect of increasing fracture number on the peak load-bearing capacity varies significantly with fracture dip angle. This effect is most pronounced at 15° and 60°, but relatively weak at 90°. The relative change rates of the modulus of elasticity are the highest at 15° and 45°, reaching 8.73% and 5.92%, respectively. This indicates that the stiffness degradation caused by double fractures is more significant than that caused by a single fracture under these dip-angle conditions. The relative change rates of microcrack number are relatively high at 0°, 45°, 75°, and 90°, suggesting that the microcrack number is more sensitive to changes in fracture number at these dip angles. The energy indices also show obvious dip-angle dependence. At 30°, the relative change rate of U_e/U is 14.93%, indicating that the weakening effect of increasing fracture number on pre-peak energy storage capacity is the most significant under this dip angle. Meanwhile, the relative change rate of U_d/U_e is −50.00%, indicating that the damage dissipation effect is further enhanced under double-fracture conditions compared with single-fracture conditions at this angle. Overall, the sensitive dip-angle ranges corresponding to different indices are not consistent. This indicates that increasing fracture number does not produce an equivalent effect at all dip angles, but shows obvious dip-angle dependence. This further demonstrates that a significant coupling effect exists between fracture number and fracture dip angle.

Table 3. Relative change rates for different indicators.

Fracture Angle	Rate of Change in Peak Stress	Rate of Change in Elastic Modulus	Rate of Change in Crack Count	Rate of Change in U_e/U	Rate of Change in U_d/U_e
0°	8.29%	1.82%	19.45%	−2.13%	42.86%
15°	20.80%	8.73%	12.23%	1.22%	−4.35%
30°	7.69%	3.64%	7.81%	14.93%	−50.00%
45°	9.46%	5.92%	19.36%	−12.16%	42.86%
60°	19.05%	2.38%	−3.62%	10.99%	−130.00%
75°	13.81%	4.37%	20.28%	−5.75%	40.00%
90°	3.63%	2.70%	18.10%	5.32%	−71.43%

Relative change rate analysis quantitatively characterizes the differences between single-fracture and double-fracture specimens under different dip angles and reflects the dip-angle dependence of the fracture–number effect. However, because this method is based on discrete dip-angle conditions, it cannot describe the continuous variation between fracture number and fracture dip angle. Therefore, fitting analysis was introduced to continuously characterize the response of each index with dip angle and identify the corresponding sensitive ranges. As shown in Figure 10, the low-value regions of peak strength and modulus of elasticity are mainly concentrated at 15–45°, indicating that increasing fracture number more significantly weakens the load-bearing capacity and overall stiffness of sandstone within this range. The microcrack number changes more markedly near 45°, suggesting that crack initiation and propagation are more sensitive to

fracture number. The energy indices vary most obviously near 30°, where U_e/U decreases and U_d/U_e increases significantly, indicating enhanced energy dissipation and weakened energy storage capacity. In addition, some fitting surfaces show large local gradients, suggesting that the fracture–number effect is nonuniform and may intensify local damage and instability under specific dip angles. Overall, the influence of fracture number on the mechanical properties and failure characteristics of sandstone is most significant within 15–45°, with energy dissipation most prominent at 30° and crack initiation and propagation most sensitive at 45°. Thus, 15–45° can be regarded as the sensitive range for fracture–number-induced damage and instability.

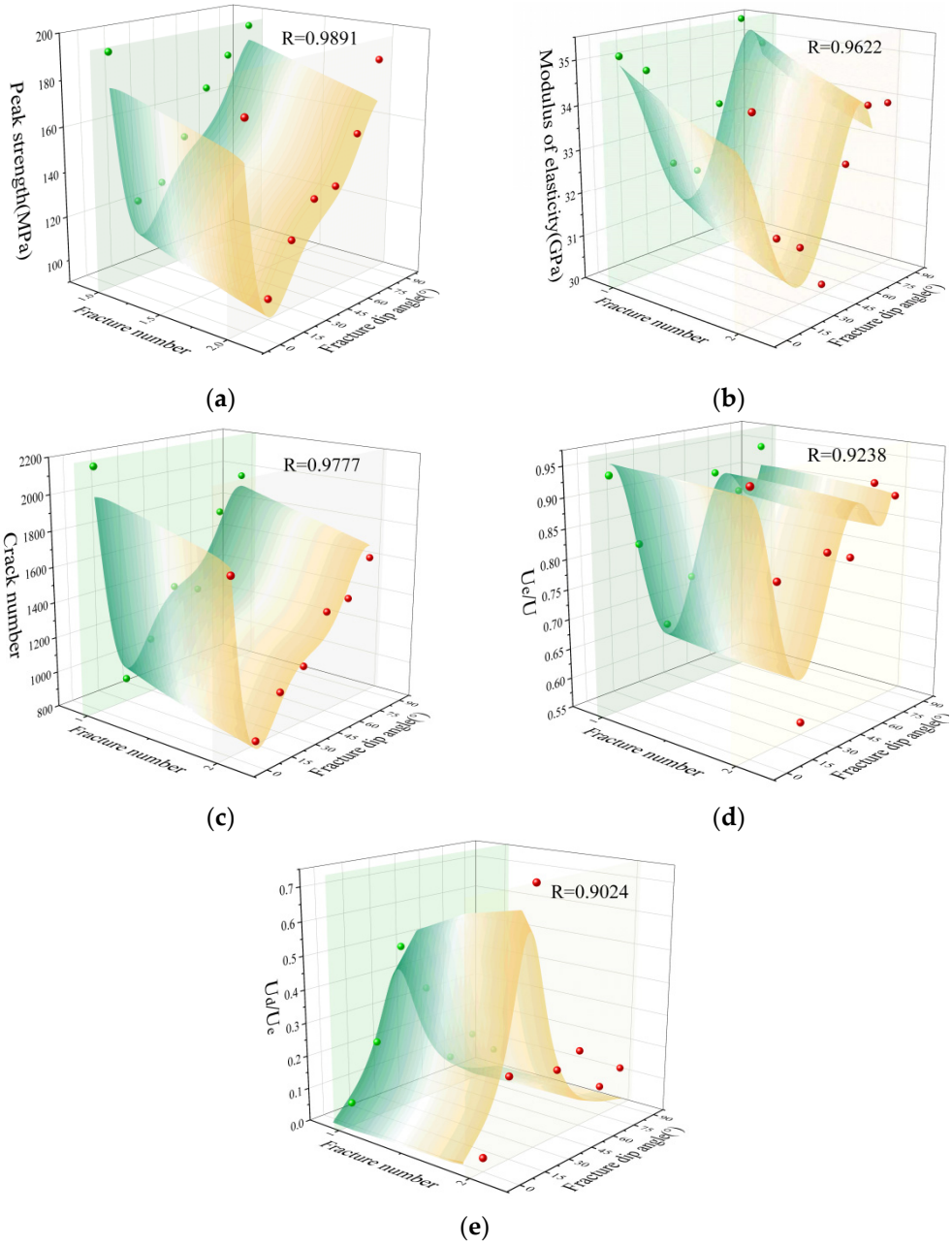

Figure 10. Three-dimensional fitting surfaces of various parameters in sandstone as a function of fracture number and dip angle. (**a**) peak stress, (**b**) Modulus of elasticity, (**c**) Crack number, (**d**) U_e/U, (**e**) U_d/U_e.

Combining the relative change rate analysis and fitting results, a clear coupling effect exists between fracture number and fracture dip angle. The influence of increasing

fracture number on sandstone failure behavior varies with fracture dip angle, rather than remaining constant under all dip-angle conditions. This coupling effect is not reflected by synchronous enhancement of all indices, but by differentiated responses of different failure behaviors within different dip-angle ranges. In particular, 15–45° is the main range where the fracture–number effect is significant, characterized by reduced load-bearing capacity, weakened stiffness, and enhanced energy dissipation. This indicates that sandstone strength degradation, microcrack development, and energy dissipation are jointly controlled by fracture number and fracture dip angle.

4.2. Effects of Fracture Number and Dip Angle on Principal Load Paths and Force Chain Evolution

The above relative change rate analysis and fitting surfaces reveal the differentiated variations in each index under the combined effects of fracture number and fracture dip angle. However, based only on strength, microcrack number, and energy indices, it remains difficult to further explain the formation mechanisms of load-bearing capacity reduction, localized crack evolution, and differences in energy storage and dissipation under different dip angles. During loading, rock transmits external loads through its internal load-bearing skeleton, and the strong force chain is an important mesoscopic indicator of this skeleton. Its continuity, spatial distribution, and concentration near fracture tips can reflect whether the main load-bearing path is complete, whether local damage is concentrated, and whether the energy storage condition is stable. Therefore, a strong force chain analysis was further conducted to explain the causes of sandstone strength degradation, crack distribution differences, and energy evolution differences under the combined effects of fracture number and fracture dip angle. In the specific analysis process, force-chain spatial distribution identification was combined with quantitative indices. Based on the force-chain distribution at the peak stress state, the main load-bearing paths and force-chain characteristics were identified. Meanwhile, high-strength force chains were extracted according to the contact normal force amplitude. The fracture resistance index R and the local strong force-chain density ρ_s were then introduced to characterize the preservation degree of the global load-bearing skeleton and the concentration degree of high-strength force chains near fracture tips, respectively. By combining the force-chain distribution pattern with these quantitative indices, the degradation of sandstone load-bearing capacity and the differences in failure behavior under different combinations of fracture number and fracture dip angle can be further analyzed.

This study is based on a statistical method for force chains derived from particle contact forces. Within a predefined sampling region Ω, force chains are quantitatively analyzed from the contact surfaces. All particle–particle contacts where the contact position x_c falls within Ω constitute the set C_Ω. For each contact c, the normal contact force $F_n(c)$ is extracted, and its magnitude is defined as $F(c) = |F_n(c)|$. The average magnitude of the normal forces within region Ω is defined as Equation (11):

$$\overline{F}_\Omega = \frac{1}{|C_\Omega|} \sum_{c \in C_\Omega} F(c) \tag{11}$$

When the magnitude of a contact force exceeds a threshold proportional to the average value, the contact is classified as a strong contact. This criterion is defined in Equation (12):

$$F_C \geq \alpha \overline{F}_\Omega \tag{12}$$

α is a preset coefficient (taken as $\alpha = 1.5$ in this paper), representing the criterion for distinguishing high-strength force chains from ordinary contacts. Therefore, the total

number of force chain elements and the number of high-strength force chain elements within region Ω are calculated as $N_{total} = |C_\Omega|$ and $N_{HF} = |C_\Omega{}^{HF}|$, respectively.

Figure 11 shows that the combined effects of fracture number and fracture dip angle change the force chain distribution and main load-bearing paths at the peak stress. In the intact specimen, the force chains are relatively uniformly distributed, and the load-bearing skeleton is continuous. Thus, the external load can be transmitted through relatively complete paths inside the specimen. With increasing fracture number, the main load-bearing paths are deflected, weakened, or locally interrupted near the fractures. The additional fracture further cuts and disperses the load-bearing paths, reducing the continuity of the force chain network at the peak stress. As the fracture dip angle increases, the force chains are redistributed near the two fracture tips and potential coalescence paths, and the spatial morphology of the main load-bearing paths is adjusted accordingly. Therefore, fracture number mainly weakens the overall integrity of the load-bearing skeleton, whereas fracture dip angle further regulates the spatial distribution of high-intensity force chains.

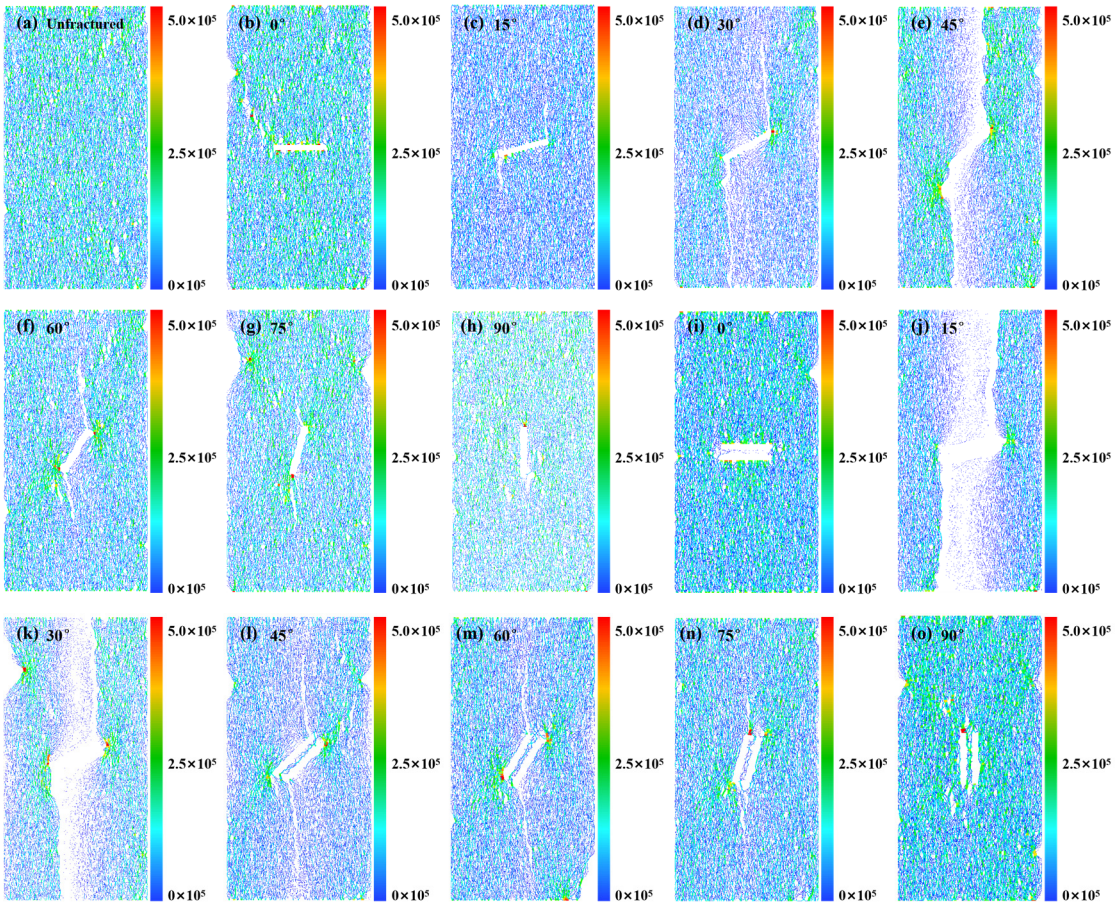

Figure 11. Force chain distribution at the peak point.

The differences in energy evolution can be further explained from the perspective of load-bearing skeleton integrity. When the main load-bearing paths have good continuity, the input energy is more easily stored in the specimen as elastic strain energy, resulting in a higher U_e/U and a lower U_d/U_e. In contrast, when fractures cause deflection, reorganization, or local interruption of load-bearing paths, particle contact adjustment and crack propagation become more active, and more input energy participates in damage development and dissipation. The energy results show that U_e/U is lower and U_d/U_e is higher under the 30° condition, indicating that the weakening effect of fractures on pre-peak energy storage capacity and their promoting effect on dissipation are more significant at

this dip angle. These results suggest that fracture number and fracture dip angle further regulate the pre-peak energy distribution characteristics of sandstone by affecting internal load-bearing paths and local damage development.

Observing the force chain distribution diagram (Figure 11) alone can reflect the spatial variation in the load-bearing path, but it is difficult to quantitatively explain the reasons for the differences in peak load-bearing capacity under different inclination angles. Previous results indicate that the specimen exhibits the lowest peak stress at 15°, and that peak stress critically depends on whether high-strength load-bearing chains can remain continuous during crack propagation at the moment of peak stress. Based on this, this paper adopts the definition proposed by Zhang et al. [37] and introduces the fracture resistance index R to characterize the retention level of high-strength load-bearing chains relative to the number of cracks. Accordingly, the fracture resistance index is defined as given in Equation (13):

$$R = \frac{N_{HF}}{N_C} \tag{13}$$

N_{HF} represents the number of high-strength force chains that satisfy the unified threshold condition at the peak moment, and N_C represents the total number of microcracks in the specimen at the same moment. To ensure comparability across different fracture dip angles, both force chain and microcrack-related indices are extracted at the peak stress point. Since R reflects the retention degree of high-strength load-bearing force chains relative to microcrack damage, a higher R value indicates that the specimen still retains more high-strength load-bearing paths at the peak point. This implies that the weakening effect of microcrack coalescence on the primary load-bearing skeleton is relatively low, and the specimen exhibits stronger fracture resistance.

Figure 12 shows that the R values of single- and double-fracture specimens generally first decrease and then increase. They remain in a low-value range near 15° and are relatively higher at 0° and 90°. This pattern is generally consistent with the variation trend of peak strength with fracture dip angle. At 15°, the R values of both single- and double-fracture specimens are relatively low. This indicates that, although the total number of microcracks is small at this dip angle, the retention capacity of high-strength load-bearing force chains is weaker. Once microcracks concentrate and develop near the pre-existing fractures, they are more likely to disrupt the primary load-bearing skeleton, which explains the lowest peak strength observed in the preceding results. In contrast, the higher R values at 0° and 90° indicate that the strong force chain skeleton is better preserved at the peak stress, allowing the specimens to maintain relatively high peak load-bearing capacity. In addition, the R values of double-fracture specimens are lower than those of single-fracture specimens, suggesting that increasing fracture number further weakens the continuity of the main load-bearing skeleton and thus reduces the overall peak load-bearing capacity. This phenomenon also helps explain the more pronounced strength deterioration observed in double-fracture specimens. Taking the 15° condition as an example, the peak strength of the single-fracture specimen was 125 MPa, whereas that of the double-fracture specimen was further reduced to 99 MPa. This value corresponds to only 51.3% of the strength of the intact sandstone. Although the final total number of microcracks in the double-fracture specimen was lower than that in the single-fracture specimen, the overall R value was also lower. This indicates that the high-strength load-bearing force-chain skeleton was more severely weakened. Due to the enhanced interaction between the two pre-existing fractures, stronger stress concentrations were developed at the crack tips. Consequently, cracks were more likely to propagate and coalesce along the existing fractures and rock-bridge regions. Compared with the single-fracture specimen, macroscopic instability occurred at an earlier stage in the double-fracture specimen. As a result, the system lost part of

its ability to further accumulate energy and generate diffuse microcracks throughout the specimen. Therefore, the failure of the double-fracture specimen was not characterized by the formation of more microcracks. Instead, it was characterized by the premature failure of the primary load-bearing force-chain skeleton under lower stress levels, which ultimately led to a more significant reduction in peak strength.

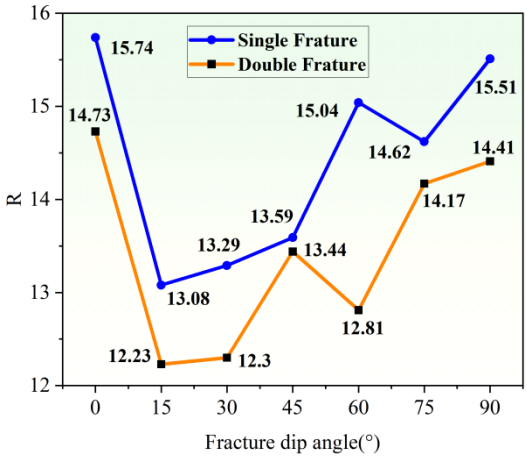

Figure 12. Variation in the fracture resistance index *R* with inclination angle.

It should be noted that *R* reflects the overall preservation state of the high-strength load-bearing skeleton at the whole-specimen scale at the peak stress. However, fracture tips and their adjacent regions are usually the most active locations for stress concentration, microcrack initiation, and propagation. Therefore, the global *R* index alone is insufficient to reveal the spatial differences in local load-bearing structures near fractures. To further analyze the local distribution characteristics of strong force chains near fracture tips, single-fracture specimens were selected, and the local strong force chain density ρ_s was introduced to quantitatively characterize the spatial distribution of strong force chains near fracture tips. In this study, statistical regions at different scales were defined with the fracture tip as the center, namely the small-scale region S-small, medium-scale region M-middle, and large-scale region B-big. The corresponding radii were set to 10 mm, 15 mm, and 20 mm, respectively, to statistically analyze the number and density distribution characteristics of strong force chains at different spatial scales. The strong force chain density is defined as given in Equation (14) [37]:

$$\rho_s = \frac{N_{HF}}{A_N} \tag{14}$$

N_{HF} represents the number of high-force chains in the rock sample, and A_N represents the area of the region.

Figure 13 shows the variation in ρ_s with fracture dip angle in different statistical regions. Overall, ρ_s is higher in the small-scale region than in the medium- and large-scale regions, indicating that strong force chains are more concentrated near the fracture tips. With increasing fracture dip angle, ρ_s generally first decreases and then increases. It remains at a relatively low level near 15° and gradually recovers under high-dip-angle conditions. This trend is generally consistent with the variations in UCS and *R* discussed above, indicating that the retention degree of the local load-bearing skeleton near fracture tips is closely related to the peak load-bearing capacity of the specimen.

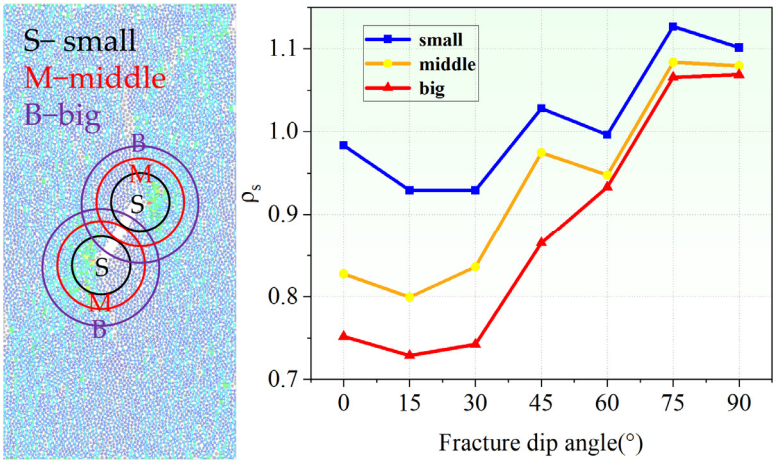

Figure 13. Schematic diagram of regional division (examples at 0° and 60°) and ρ_s varies with dip angle in different regions.

When ρ_s is high, relatively concentrated high-strength load-bearing chains remain near the fracture tips, suggesting that the local load-bearing skeleton is well preserved and that the specimen has a relatively high peak load-bearing capacity. In contrast, the decrease in ρ_s at 15° indicates that the local high-strength load-bearing structure near the fracture tips is weakened, and failure is more likely to concentrate near the pre-existing fractures. This is consistent with the previous result that the total crack number is lower at 15°, whereas the peak strength is the lowest. Therefore, *R* mainly reflects the retention level of the global main load-bearing skeleton relative to crack development, whereas ρ_s further characterizes the concentration degree of local high-strength load-bearing zones near fracture tips. These two indices explain the variations in peak strength and crack localization from global and local perspectives, respectively.

In summary, fracture number and fracture dip angle further affect the weakening of load-bearing capacity, localized crack evolution, and energy storage–dissipation distribution of sandstone by regulating the main load-bearing paths and strong force chain evolution. Increasing fracture number weakens the continuity of the load-bearing skeleton, whereas changing fracture dip angle further modifies the spatial distribution of high-strength force chains and the morphology of the main load-bearing paths, resulting in different mechanical properties and failure characteristics under different dip angles. In particular, the weakening of the load-bearing skeleton is most evident at 30°, which is manifested by reduced energy storage capacity and significantly enhanced energy dissipation. The *R* index reflects the retention capacity of the main load-bearing skeleton relative to crack damage at the global scale, while ρ_s characterizes the concentration degree of high-strength load-bearing chains near fracture tips at the local scale. A weaker local load-bearing skeleton indicates that cracks are more likely to concentrate and propagate near the fractures, leading to lower peak load-bearing capacity. Overall, the mechanical properties and failure characteristics of sandstone under different dip angles are jointly controlled by the retention capacity of the global main load-bearing skeleton and the evolution of local high-strength load-bearing zones near fracture tips.

4.3. Comparative Analysis with Existing Experimental Results

To further evaluate the rationality of the fractured models, the numerical simulation results were compared with previous experimental studies from three aspects: mechanical properties, crack propagation patterns, and energy evolution behavior. The supplementary significance of this study was also clarified.

First, fracture number and fracture dip angle show parameter-specific effects on the macroscopic mechanical properties of sandstone. Based on the force chain distribution at the peak stress, this study analyzed their effects on the mesoscopic load-bearing structure and macroscopic mechanical properties, thereby addressing the limitation of previous experimental studies that mainly focused on macroscopic phenomena. The simulation results show that increasing fracture number systematically weakens the overall load-bearing capacity and deformation resistance of sandstone. The peak stress and modulus of elasticity of single-fracture and double-fracture specimens are significantly lower than those of intact sandstone. This is consistent with the experimental results reported by Yang et al. [38] and Zhao et al. [9], in which fractures were found to weaken the mechanical properties of rock masses. More importantly, fracture dip angle has different effects on different mechanical indices. The peak stress reaches its minimum value at 15°, whereas the modulus of elasticity reaches its minimum value at 45°. This confirms that the sensitive dip angles corresponding to peak load-bearing capacity and initial stiffness are different. Unlike previous experimental studies that only described this macroscopic phenomenon, this study clarifies the underlying mechanism through mesoscopic strong force chain analysis. At a fracture dip angle of 15°, the continuity of the main load-bearing skeleton is severely disrupted, and high-strength load-bearing chains are difficult to maintain. This leads to a rapid decrease in peak load-bearing capacity and further improves the understanding of how fracture geometry controls the mechanical behavior of sandstone at the mesoscopic scale.

Second, the failure of fractured sandstone under uniaxial compression is dominated by tensile damage and shows obvious crack localization. The simulation results show that microcracks generated during the failure process of fractured sandstone are mainly tensile cracks, whereas shear cracks account for a relatively low proportion. This indicates that specimen failure is mainly controlled by tensile damage. This result is consistent with the experimental conclusions of Yang et al. [39] and Fuqi et al. [40], who reported that the uniaxial compression failure of fractured sandstone is dominated by tensile failure. Further analysis shows that fracture dip angle significantly affects both microcrack number and spatial distribution. At 15°, the total number of microcracks is relatively low, but microcracks are mainly concentrated near the tips of pre-existing fractures and their adjacent regions, showing strong localization. This phenomenon agrees with the experimental observation of Luan et al. [41], who found that crack propagation is more likely to occur at the tips of low-dip-angle fractures. Combined with the analysis of local strong force chain density, the local high-strength load-bearing structure near fracture tips is weakened at 15°, making failure more likely to concentrate near the pre-existing fractures. Therefore, microcrack number alone cannot fully characterize the damage degree. The spatial distribution of microcracks and the state of the mesoscopic load-bearing structure should also be considered.

Third, the effects of fracture number and fracture dip angle on the energy evolution of sandstone show clear coupling characteristics. Through quantitative analysis, this study clarifies their coupling relationship and overcomes the limitation of previous studies that analyzed single parameters independently. The simulation results show that increasing fracture number significantly reduces the pre-peak elastic energy storage capacity and enhances damage dissipation. This is consistent with the experimental findings of Li et al. [42] and Tian et al. [43], which indicated that fractures intensify energy dissipation. Meanwhile, both single-fracture and double-fracture specimens exhibit the lowest U_e/U and the highest U_d/U_e at a fracture dip angle of 30°. This indicates that, under this dip angle, input energy is difficult to store stably in the elastic load-bearing structure, and the specimens are more likely to enter a pre-peak stage with enhanced dissipation. This is highly consistent with the energy evolution patterns reported by Qin et al. [44]

and Yu et al. [45]. To further explain the reasons for the differences in strength, elastic modulus, and energy storage capacity under different fracture dip angles, the microcrack distribution, energy evolution, and force-chain distribution at the peak stress state were analyzed together. The fracture dip angle changes the relative relationship between the prefabricated fracture and the loading direction. Thus, the stress concentration near fracture tips, the spatial distribution of strong force chains, and the crack propagation path are affected.

At 15°, the specimen shows the lowest peak strength. Although the final number of microcracks is relatively small under this condition, the cracks are mainly concentrated at and near the prefabricated fracture tips. This indicates a clear localized damage feature. Meanwhile, both the fracture resistance index R and the local strong force-chain density ρ_s are at relatively low levels. This indicates that the retention capacity of the main load-bearing skeleton and the aggregation degree of strong force chains near fracture tips are both weakened. Therefore, local coalescence failure can occur at a lower stress level, resulting in a lower peak load-bearing capacity.

At 45°, the elastic modulus reaches the minimum value. This indicates that the overall deformation resistance of the specimen is significantly weakened under this dip angle. From the force-chain distribution at the peak stress state, strong force chains show obvious deflection and local interruption near the fractures. The connectivity of the axial load-bearing path is relatively weak, indicating that the main load-bearing structure is strongly disturbed by the fractures. This force-chain distribution feature corresponds well with the lower elastic modulus at 45°.

At 30°, the energy storage capacity of the specimen is the weakest, as shown by the lowest U_e/U and the highest U_d/U_e. This indicates that the proportion of input energy converted into elastic energy is the lowest, while the proportion of dissipated energy used for damage evolution is the highest. Combined with the crack propagation and force-chain distribution results, crack propagation at and near the fracture tips is relatively evident under this dip angle. The local load-bearing structure is weakened, making it difficult for the input energy to be continuously stored in the elastic load-bearing structure. It should be noted that the energy indices reflect the cumulative process of energy storage and dissipation during loading. They are not completely equivalent to the continuity of force chains at the peak stress state. Therefore, the weaker energy storage capacity at 30° mainly reflects a more significant pre-peak damage dissipation process.

Furthermore, the relative change rate η and fitting surface analysis were used to quantitatively characterize the dip-angle dependence of the fracture–number effect. Under different fracture dip angles, the weakening degrees of fracture number on strength, stiffness, and energy indices are clearly different. This indicates that the effects of fracture number and fracture dip angle on sandstone failure behavior are not a simple superposition. Instead, they jointly influence strength degradation, crack development, and energy evolution. This result provides a quantitative basis for further understanding the mechanical properties and energy evolution characteristics of sandstone under combined fracture geometries.

Overall, the simulation results of this study are in good agreement with previous experimental studies in terms of peak stress, modulus of elasticity, microcrack propagation, and energy evolution. On this basis, the relationships between macroscopic mechanical behavior and mesoscopic load-bearing structure of sandstone under different combinations of fracture number and fracture dip angle were analyzed by combining mechanical properties, microcrack distribution, energy allocation, and force chain characteristics at the peak stress. The results show that the combined effects of fracture number and fracture dip angle have significant coupling effects on strength degradation, crack localization, and energy dissipa-

tion in sandstone. An increase in fracture number can be regarded as an important indicator for identifying weakened load-bearing capacity in deep roadways surrounding rocks. For strength degradation and local failure near fracture tips, low-dip-angle fractures should be given particular attention. For pre-peak damage accumulation and enhanced energy dissipation, fractures with a dip angle of 30° should be emphasized. For surrounding-rock stiffness degradation and deformation sensitivity, fractures with a dip angle of 45° should be considered critical. These results can provide a reference for damage assessment of deep surrounding rocks, identification of unfavorable fracture geometries, determination of weak load-bearing zones, and selection of key support areas. They also indicate that the combined effects of fracture number and fracture dip angle should be comprehensively considered in engineering analysis to more accurately evaluate surrounding-rock stability.

4.4. Limitations of This Study

Several limitations still exist in this study. First, the numerical model was mainly validated using the peak uniaxial compressive strength and comparisons with previous studies. Due to the limited availability of experimental data, more comprehensive validation is still needed. In future work, full stress–strain curves, modulus of elasticity, failure mode, crack patterns, Brazilian tensile strength, and triaxial test results should be considered for model validation.

Second, this study was conducted based on two-dimensional PFC simulations. Although the 2D model can reveal the effects of fracture number and fracture dip angle on the failure behavior of sandstone, the three-dimensional fracture geometry cannot be fully represented. Out-of-plane crack propagation and spatial stress redistribution in real rock masses also cannot be fully captured. Therefore, the present findings should be further verified and extended by three-dimensional numerical simulations and laboratory tests.

Third, the fracture number considered in this study was limited to intact, single-fracture, and double-fracture specimens. Therefore, the conclusions regarding fracture number effects are applicable only to the fracture configurations considered in this study. More complex fracture configurations, such as triple-fracture and multi-fracture models, should be considered in future studies.

5. Conclusions

In this study, uniaxial compression models of intact sandstone, single-fracture sandstone, and double-fracture sandstone were established using PFC^{2D}. The individual and coupled effects of fracture number and fracture dip angle were systematically analyzed from the perspectives of mechanical properties, microcrack evolution, and energy distribution. The differentiated laws of sandstone strength degradation, microcrack propagation, and energy dissipation under different fracture numbers and dip angles were revealed. The main conclusions are as follows:

(1) In terms of mechanical properties, increasing fracture number weakens the load-bearing capacity and deformation resistance of sandstone, resulting in decreases in peak stress and modulus of elasticity. Fracture dip angle has different controlling effects on strength and stiffness. The peak stress reaches its minimum value at 15°, whereas the modulus of elasticity reaches its minimum value at 45°. Their coupling effect is manifested by the variation in the weakening degree caused by fracture number with fracture dip angle. The weakening of peak stress is most significant at 15° and 60°, while the weakening of modulus of elasticity is more obvious at 15° and 45°. The fitting surfaces also show that strength and stiffness are generally lower within the range of 15–45°, indicating that increasing fracture number is more likely to weaken the mechanical properties of sandstone within this dip-angle range.

(2) In terms of microcrack evolution, increasing fracture number reduces the total number of microcracks but makes crack propagation more localized. This indicates that sandstone failure becomes more dependent on local crack propagation and the development of the main failure path with increasing fracture number. Fracture dip angle mainly controls the spatial distribution of cracks. For example, under the 15° condition, cracks are concentrated near the pre-existing fractures, showing obvious localization characteristics. The coupling effect between fracture number and fracture dip angle is reflected by the variation in the reduction degree of microcrack number with dip angle when the specimen changes from a single-fracture to a double-fracture condition. The differences in microcrack number between single-fracture and double-fracture specimens are relatively large at 0°, 45°, 75°, and 90°, indicating that microcrack number is more sensitive to fracture number at these dip angles.

(3) In terms of energy evolution, increasing fracture number generally reduces the elastic strain energy level at the peak point, indicating that additional fractures weaken the ability of the specimen to maintain elastic energy storage. Fracture dip angle mainly affects the distribution relationship between elastic energy storage and damage dissipation. Both single-fracture and double-fracture specimens show the lowest U_e/U and the highest U_d/U_e at 30°, indicating that input energy is most difficult to store as elastic strain energy at this dip angle and is more likely to be converted into damage dissipation. Their coupling effect is reflected by the clear dip-angle dependence of the fracture–number effect. When the specimen changes from a single-fracture to a double-fracture condition, the dissipation effect is relatively enhanced at some dip angles, including 15°, 30°, 60°, and 90°, but relatively weakened at others, including 0°, 45°, and 75°. This indicates that increasing fracture number does not uniformly enhance damage dissipation, but is jointly controlled by fracture dip angle.

Author Contributions: Conceptualization, B.L., Z.L. and X.C.; Methodology, J.L., B.L., X.Z. and Y.L.; Software, J.L., X.Z. and M.Z.; Validation, X.C., X.Z., N.L. and M.Z.; Formal analysis, J.L., Y.L. and N.L.; Investigation, X.L.; Resources, Z.L. and X.L.; Writing—original draft, J.L.; Writing—review and editing, B.L., Z.L., X.C., Y.L., N.L., M.Z. and X.L.; Visualization, Z.L.; Funding acquisition, B.L. All authors have read and agreed to the published version of the manuscript.

Funding: National Natural Science Foundation of China, Grant Number: 52304260, 52574258. Key Technologies R&D Program of Shanxi Province, China, Grant Number: 202402100101002. State-funded Postdoctoral Fellowship Program, Grant Number: GZC20241583. State Key Laboratory Cultivation Base for Gas Geology and Gas Control (Henan Polytechnic University), Grant Number: WS2025B06.

Institutional Review Board Statement: Not applicable.

Informed Consent Statement: Not applicable.

Data Availability Statement: The data that support the findings of this study are available from the corresponding author upon reasonable request.

Conflicts of Interest: The authors declare no conflicts of interest.

References

1. Li, X.L.; Chen, S.J.; Liu, S.M.; Li, Z.H. AE waveform characteristics of rock mass under uniaxial loading based on Hilbert-Huang transform. *J. Cent. South Univ.* **2021**, *28*, 1843–1856. [CrossRef]
2. Li, X.L.; Chen, S.J.; Li, Z.H.; Wang, E.Y. Rockburst mechanism in coal rock with structural surface and the microseismic (MS) and electromagnetic radiation (EMR) response. *Eng. Fail. Anal.* **2021**, *124*, 105396. [CrossRef]
3. Li, X.L.; Wang, E.Y.; Li, Z.H.; Liu, Z.T.; Song, D.Z.; Qiu, L.M. Rock burst monitoring by integrated microseismic and electromagnetic radiation methods. *Rock Mech. Rock Eng.* **2016**, *49*, 4393–4406. [CrossRef]

4. Xia, Z.J.; Yuan, H.P.; Li, H.Z.; Yu, X.Y.; Fang, X.Y.; Huang, S.T. Energy Transfer and Damage Evolution Process Research of Ore Rock-Filling Body under the Blasting Load. *Minerals* **2022**, *12*, 1362. [CrossRef]
5. Liu, S.M.; Sun, H.T.; Zhang, D.M.; Yang, K.; Li, X.L.; Wang, D.K.; Li, Y.N. Experimental study of effect of liquid nitrogen cold soaking on coal pore structure and fractal characteristics. *Energy* **2023**, *275*, 127470. [CrossRef]
6. Wang, X.F.; Xia, Z.G.; Li, P.; Liu, H.N. Numerical study on strength and failure behavior of rock with composite defects under uniaxial compression. *Energies* **2021**, *14*, 4418. [CrossRef]
7. Haeri, H.; Sarfarazi, V.; Marji, M.F. Static and Dynamic response of rock engineering models. *Iran. J. Sci. Technol. Trans. Civ. Eng.* **2022**, *46*, 327–341. [CrossRef]
8. Chen, W.; Wan, W.; Zhao, Y.L.; Peng, W.Q. Experimental study of the crack predominance of rock-like material containing parallel double fissures under uniaxial compression. *Sustainability* **2020**, *12*, 5188. [CrossRef]
9. Zhao, Y.Q.; Li, Q.S.; Zhang, K.; Yang, Y.M.; Gu, X.B. Effect of fissure angle on energy evolution and failure characteristics of fractured rock under uniaxial cyclic loading. *Sci. Rep.* **2023**, *13*, 2678. [CrossRef] [PubMed]
10. Feng, P.; Dai, F.; Liu, Y.; Xu, N.W.; Zhao, T. Influence of two unparallel fissures on the mechanical behaviours of rock-like specimens subjected to uniaxial compression. *Eur. J. Environ. Civ. Eng.* **2020**, *24*, 1643–1663. [CrossRef]
11. Zhang, X.P.; Liu, Q.S.; Wu, S.C.; Tang, X.H. Crack coalescence between two non-parallel flaws in rock-like material under uniaxial compression. *Eng. Geol.* **2015**, *199*, 74–90. [CrossRef]
12. Wong, R.H.C.; Chau, K.T.; Tang, C.A.; Lin, P. Analysis of crack coalescence in rock-like materials containing three flaws—Part I: Experimental approach. *Int. J. Rock Mech. Min. Sci.* **2001**, *38*, 909–924. [CrossRef]
13. Dai, B.; Chen, Y.; Zhao, G.Y.; Liang, W.Z.; Wu, H. A Numerical Study on the Crack Development Behavior of Rock-Like Material Containing Two Intersecting Flaws. *Mathematics* **2019**, *7*, 1223. [CrossRef]
14. Lian, S.L.; Wan, W.; Zhao, Y.L.; Wu, Q.H.; Du, C. Investigation of the mechanical behavior of rock-like material with two flaws subjected to biaxial compression. *Sci. Rep.* **2024**, *14*, 14136. [CrossRef] [PubMed]
15. Zhang, L.R.; Nguyen, N.G.H.; Lambert, S.; Nicot, F.; Prunier, F.; Djeran-Maigre, I. The role of force chains in granular materials: From statics to dynamics. *Eur. J. Environ. Civ. Eng.* **2016**, *21*, 874–895. [CrossRef]
16. Zhang, M.; Konietzky, H.; Song, Z. Evolution of force network, contact network, and tensile force chains in rock-like bonded granular materials under unconfined and confined compression: A DEM study. *Environ. Earth Sci.* **2025**, *84*, 320. [CrossRef]
17. Wang, M.M.; Wang, J.A.; Li, F.; Liang, C.; Yang, L. Arching of force chains in excavated granular material. *Front. Earth Sci.* **2024**, *11*, 1322038. [CrossRef]
18. McBeck, J.; Mair, K.; Renard, F. How porosity controls macroscopic failure via propagating fractures and percolating force chains in porous granular rocks. *J. Geophys. Res. Solid Earth* **2019**, *124*, 9920–9939. [CrossRef]
19. Thompson, N.; Bennett, M.R.; Petford, N. Analyses on granular mass movement mechanics and deformation with distinct element numerical modeling, implications for large-scale rock and debris avalanches. *Acta Geotech.* **2009**, *4*, 233–247. [CrossRef]
20. Wang, Y.F.; Cui, F. Energy evolution mechanism in process of sandstone failure and energy strength criterion. *J. Appl. Geophys.* **2018**, *154*, 21–28. [CrossRef]
21. Ríos-Bayona, F.; Johansson, F.; Mas-Ivars, D.; Sánchez-Juncal, A.; Bolin, A. Using PFC2D to simulate the shear behaviour of joints in hard crystalline rock. *Bull. Eng. Geol. Environ.* **2022**, *81*, 381. [CrossRef]
22. Rezaee, H.; Noorian-Bidgoli, M. Numerical and experimental investigations of grain size and temperature effects on the crack propagation velocity in brittle rocks. *Comput. Part. Mech.* **2025**, *12*, 2969–2981. [CrossRef]
23. Bahaaddini, M.; Sheikhpourkhani, A.M.; Mansouri, H. Flat-joint model to reproduce the mechanical behaviour of intact rocks. *Eur. J. Environ. Civ. Eng.* **2019**, *25*, 1427–1448. [CrossRef]
24. Yang, Y.S.; Cheng, S.P.; Zhang, Z.R.; Yin, M.Y.; Hou, J.W. Study on the stress field concentration at the tip of elliptical cracks. *Rev. Adv. Mater. Sci.* **2022**, *61*, 611–621. [CrossRef]
25. Guo, P.Y.; Zhang, P.; Bu, M.H.; Wang, J.M.; Zheng, X.; He, M.C. Microcracking behavior and damage mechanism of granite subjected to high temperature based on CT-GBM numerical simulation. *Comput. Geotech.* **2023**, *159*, 105385. [CrossRef]
26. Yang, S.Q.; Yang, D.S.; Jing, H.W.; Li, Y.H.; Wang, S.Y. An experimental study of the fracture coalescence behaviour of brittle sandstone specimens containing three fissures. *Rock Mech. Rock Eng.* **2012**, *45*, 563–582. [CrossRef]
27. Ma, Z.; Wang, H.B.; Wang, C.G.; Yu, Z.H. Creep characteristics of corn straw particles simulated based on Burgers model. *Bioresources* **2024**, *19*, 53–65. [CrossRef]
28. Ajamzadeh, M.R.; Sarfarazi, V.; Haeri, H.; Dehghani, H. The effect of micro parameters of PFC software on the model calibration. *Smart Struct. Syst.* **2018**, *22*, 643–662. [CrossRef]
29. Yu, C.; Zhang, C.; Han, T.; Cao, X.J.; Zhao, Y.J.; Pan, Y.T. Macro–Meso-Parameter Calibration of Green Sandstone via XGBoost Screening and Stepwise Regression with Application to Impact-Fragmentation Analysis. *Minerals* **2026**, *16*, 490. [CrossRef]
30. Xu, Z.H.; Wang, Z.Y.; Wang, W.Y.; Lin, P.; Wu, J. An integrated parameter calibration method and sensitivity analysis of microparameters on mechanical behavior of transversely isotropic rocks. *Comput. Geotech.* **2022**, *142*, 104573. [CrossRef]

31. Miao, L.L.; Liu, X.R.; Fu, Y. Approach for determining micro-strength parameters of rock based on particle flow code. *Sci. Rep.* **2024**, *14*, 11230. [CrossRef] [PubMed]
32. Yang, S.Q.; Huang, Y.H.; Ranjith, P.G.; Jiao, Y.Y.; Ji, J. Discrete element modeling on the crack evolution behavior of brittle sandstone containing three fractures under uniaxial compression. *Acta Mech. Sin.* **2015**, *31*, 871–889. [CrossRef]
33. Li, H.T.; Li, X.L.; Fu, J.H.; Zhu, N.Q.; Chen, D.Y.; Wang, Y.; Ding, S. Experimental study on compressive behavior and failure characteristics of imitation steel fiber concrete under uniaxial load imitation steel fiber concrete under uniaxial load. *Constr. Build. Mater.* **2023**, *399*, 132599. [CrossRef]
34. Xu, D.K.; Mu, C.M.; Zhang, W.Q.; Li, Z.Q. Research on energy dissipation laws of coal crushing under the impact loads. *Shock Vib.* **2021**, *2021*, 5563196. [CrossRef]
35. Dai, B.; Zhao, G.F.; Zhang, L.; Liu, Y.; Zhang, Z.J.; Luo, X.Y.; Chen, Y. Energy dissipation of rock with different parallel flaw inclinations under dynamic and static combined loading. *Mathematics* **2022**, *10*, 4082. [CrossRef]
36. Yu, J.; Yao, Y.L.; Xu, T.F.; Shang, A.F.; Wang, K.Z. Evaluation of the strength and brittleness of mortar containing fissures and rubber. *Constr. Build. Mater.* **2025**, *464*, 140091. [CrossRef]
37. Zhang, T.; Yu, L.Y.; Ma, L.J.; Tan, Y.Z.; Li, W.; Fan, D.D.; Mi, X.Z. Numerical investigation of the three dimensional multi-level force chain network of the sample with a single fissure under uniaxial compression. *Theor. Appl. Fract. Mech.* **2024**, *130*, 104345. [CrossRef]
38. Yang, S.Q.; Jing, H.W. Strength failure and crack coalescence behavior of brittle sandstone samples containing a single fissure under uniaxial compression. *Int. J. Fract.* **2011**, *168*, 227–250. [CrossRef]
39. Yang, S.Q.; Tian, W.L.; Huang, Y.H.; Ranjith, P.G.; Ju, Y. An Experimental and Numerical Study on Cracking Behavior of Brittle Sandstone Containing Two Non-coplanar Fissures Under Uniaxial Compression. *Rock Mech. Rock Eng.* **2015**, *49*, 1497–1515. [CrossRef]
40. Cheng, F.Q.; Li, Z.H.; Li, G.A.; Wei, Y.; Yin, S.; Liu, S.J.; Kong, Y.H. Influence of prefabricated fissure angle on sandstone damage and infrared radiation temperature characteristics. *J. Geophys. Eng.* **2018**, *15*, 1187–1196. [CrossRef]
41. Luan, Y.Q.; Liu, Z.H.; Song, G.L.; Zhang, J.P.; Chen, L.X.; Qin, P.; Liu, C.X. Relationship between mechanical properties of saturated fissured sandstone and fissure angle after freeze-thaw cycles. *Adv. Mater. Sci. Eng.* **2022**, *2022*, 6426279. [CrossRef]
42. Li, X.W.; Yao, Z.S.; Liu, X.H.; Huang, X.W. Energy evolution and damage mechanism of fractured sandstone with different angles. *Energies* **2022**, *15*, 1518. [CrossRef]
43. Tian, X.Y.; Zhao, F.J.; Wang, W.J.; Chen, B.; Ma, Y.J.; Fan, B.J. Study on energy evolution and fractal characteristics of sandstone with different fracture dip angles under uniaxial compression. *Sci. Rep.* **2024**, *14*, 10464. [CrossRef] [PubMed]
44. Qin, T.Z.; Li, L.H.; Nie, C.Y.; Zhou, J.W.; Liu, Q.Z.; Cheng, L. Study on the influence of fracture geometric characteristics on the microscopic crack propagation and energy release mechanism in granite. *Sci. Rep.* **2025**, *15*, 35293. [CrossRef] [PubMed]
45. Yu, Y.J.; Song, Z.Y.; Liu, J.M.; Yang, Y.T.; Dong, X. Energy evolution mechanism of structural surfaces in sandstones with different dips based on the energy principle. *PLoS ONE* **2024**, *19*, e0300931. [CrossRef] [PubMed]

Disclaimer/Publisher's Note: The statements, opinions and data contained in all publications are solely those of the individual author(s) and contributor(s) and not of MDPI and/or the editor(s). MDPI and/or the editor(s) disclaim responsibility for any injury to people or property resulting from any ideas, methods, instructions or products referred to in the content.